

**CIRCULATION COPY  
SUBJECT TO RECALL  
IN TWO WEEKS**

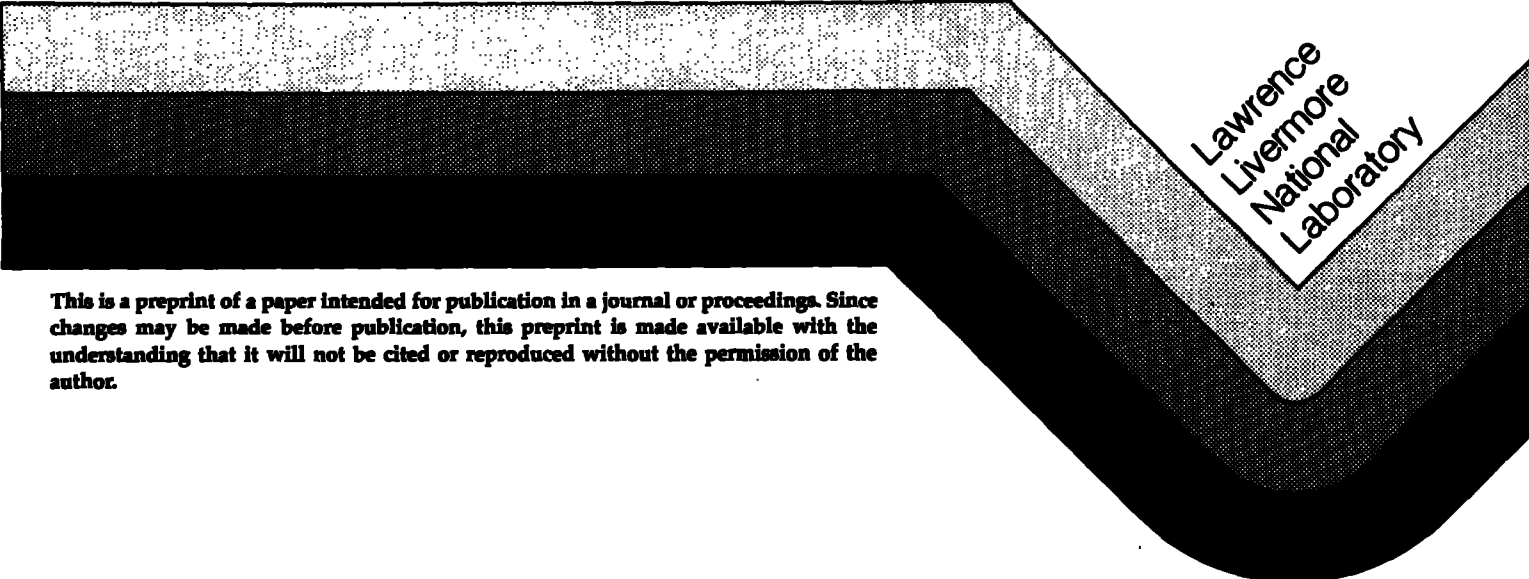
**UCRL-93161  
PREPRINT**

**A SMALL, OCTOPOLE-STABILIZED  
TANDEM MIRROR REACTOR**


**R. S. Devoto, D. E. Baldwin, E. B. Hooper,  
B. G. Logan, G. W. Hamilton, & B. M. Johnston**

**This paper was prepared for submittal to  
JOURNAL OF NUCLEAR FUSION**

**August 1, 1985**



**Lawrence  
Livermore  
National  
Laboratory**



**This is a preprint of a paper intended for publication in a journal or proceedings. Since changes may be made before publication, this preprint is made available with the understanding that it will not be cited or reproduced without the permission of the author.**

#### DISCLAIMER

This document was prepared as an account of work sponsored by an agency of the United States Government. Neither the United States Government nor the University of California nor any of their employees, makes any warranty, express or implied, or assumes any legal liability or responsibility for the accuracy, completeness, or usefulness of any information, apparatus, product, or process disclosed, or represents that its use would not infringe privately owned rights. Reference herein to any specific commercial products, process, or service by trade name, trademark, manufacturer, or otherwise, does not necessarily constitute or imply its endorsement, recommendation, or favoring by the United States Government or the University of California. The views and opinions of authors expressed herein do not necessarily state or reflect those of the United States Government or the University of California, and shall not be used for advertising or product endorsement purposes.

# A SMALL, OCTOPOLE-STABILIZED TANDEM MIRROR REACTOR\*

R. S. Devoto, D. E. Baldwin, E. B. Hooper, B. G. Logan,  
G. W. Hamilton and B. M. Johnston

Lawrence Livermore National Laboratory, University of California  
Livermore, CA 94550

## ABSTRACT

It is shown that the use of octopole stabilization in a tandem mirror reactor allows a large reduction in end-cell length. A novel feature of the method proposed in this report is the placement of the minimum  $|B|$  region considerably off axis, thus rendering the core plasma more axisymmetric. The region from the core to the field minimum is bridged by a hot-electron mantle. Low  $\beta$ , ideal magnetohydrodynamic stability, as evaluated with the interchange criterion, yields typically an upper limit to the required mantle  $\beta$  of 78% for a center-cell peak  $\beta$  of 75% and barrier peak  $\beta$  of 30%. Estimates for the worst type of classical radial diffusion - stochastic - show that radial losses are minimal for this configuration. First calculations of power balance indicate  $Q \sim 10$  for a reactor producing 500 MW of fusion power and  $Q \sim 25$  for one producing 1000 MW, using conservative assumptions regarding mantle  $\beta$  requirements and synchrotron radiation losses.

\*Work performed under the auspices of the U.S. Department of Energy by the Lawrence Livermore National Laboratory under contract number W-7405-ENG-48.

## I. INTRODUCTION

A number of modifications of the tandem mirror have been suggested since it was proposed by Dimov et al. [1] and by Fowler and Logan [2]. Conceptual designs of reactors in the original form showed that very high neutral beam energies ( $\sim 1$  MeV) and magnetic fields ( $\sim 15$  T) would be required in the quadrupole end plugs. The beam energy can be reduced to about 500 keV with the addition of electron cyclotron heating (ECH) of the plug electrons [1,3]. A reduction of the density in the plug and thus of the magnetic field can be obtained with the addition of a thermal barrier between the central-cell electrons and the potential-forming ECH electrons in the end cell [4]. As an additional feature, Kesner [5] has proposed the use of sloshing ions in an axisymmetric cell located on the central-cell side of the quadrupole anchor. The central cell ions would be reflected in the axisymmetric field and thus be free of radial transport due to the asymmetry of the quadrupole field. However, this arrangement is predicted to be unstable to trapped-particle modes [6]. Tests of this concept are currently underway in the TARA experiment [7].

An alternate method of reducing radial transport was adopted for the MARS reactor design [8]. The basic yin-yang arrangement in the end cells was extended and modified to reduce the radial transport to near zero. Since the radial deflection of a central-cell ion is proportional to a path integral of the geodesic curvature  $\Omega$ , this curvature component was adjusted with additional coils to yield a zero integral for the central-cell ions reflecting in the end cell. A total of six C-shaped coils was required in each end cell. As a result, the main end-cell length is 21.8 m with an additional 4.5 m needed to recircularize the flux for the direct converter.

A long end cell has two disadvantages. First, the loss rate of center-cell (fuel) ions due to trapping in the end cell is proportional to the end-cell length. The 21.8 m length in MARS requires center-cell lengths  $> 100$  m for alpha-particle heating to balance the trapping losses, i.e., to obtain ignition of the center cell [9]. Second, the long MARS end cells result in large magnet costs, which in turn requires a large central-cell fusion power to achieve reasonable capital cost per power output.

Although subsequent studies have indicated that some reduction could be made in the end-cell length, a very large reduction is necessary for reactors with smaller fusion power. Since a large reduction in the length of the yin-yang end cells does not appear possible, designing an economical reactor with lower fusion power necessitated looking at alternatives to quadrupole stabilization. A possible stabilization method uses higher-order multipoles obtained with multiple conductors (Ioffe bars) in planes parallel to the principal axis. Multipoles higher than quadrupole have fields which approach zero on axis, thus rendering the core fields essentially symmetric. This feature suggests that radial transport should be less of a problem. As a result of the smaller effect near the axis, the minima in  $|B|$  occur off axis and with period  $\cos(n \theta)$  where  $2n$  is the number of bars. The near-axis multipole field varies as  $r^{n-1}$ , so the higher the number of bars, the more axisymmetric the near-axis field will be. There is, however, a limit on the number of bars which can be used because of the need for access for neutral beams, ECH and drift-pumping coils. We propose here the use of octopole fields for the stabilization. Furthermore, we propose adjusting the fields to place the minimum in magnetic field  $B$  outside of the flux tubes which link to the

center-cell plasma, bridging the region between the core and the minimum- $|B|$  region with a mantle of hot, nearly constant-pressure electrons.

The concept can be more clearly explained with the aid of Fig. 1, which shows the magnetic field,  $|B|$ , and electrostatic potential,  $\phi$ , along the principal axis, and Fig. 2, which gives a schematic picture of the radial variation of  $B$  and plasma pressure,  $p = p_{||} + p_{\perp}$ , in the center and end cells. In the center cell, the plasma pressure decreases with radius (or magnetic flux  $\psi = r^2 B/2$ ) while  $B$  is nearly constant. This core plasma maps to the end cell where the field on average decreases with radius. The criterion for local flute stability of low- $\beta$  plasmas with the paraxial approximation to the magnetic field, and neglecting finite-Larmor-radius (FLR) and wall effects, is

$$\int_{-L/2}^{L/2} \frac{\kappa}{rB^2} \frac{\partial p}{\partial \psi} ds < 0 \quad (1)$$

where  $\kappa$  is the normal curvature of the vacuum field and the integral runs over the entire length,  $L$ , of the machine. In the essentially axisymmetric core plasma, on the average  $\kappa < 0$  in the plugs and central cell, and the above criterion would not be satisfied if  $\partial p / \partial \psi < 0$ . To satisfy Ineq. (1), we add sufficient plasma pressure to form a positive pressure gradient in the end cell out to the edge of the core, as indicated in Fig. 2. If the gradient is large enough, it will satisfy Ineq. (1) and ensure interchange stability. Note that the region of positive pressure gradient extends axially over a limited length of the end cell; the pressure gradient must be large enough to balance out the negative gradients in other portions of each field line in the core. From the edge of the core to the region of positive curvature, i.e., minimum  $|B|$ , the gradient can be zero or very small but positive according to Ineq. (1).

Satisfaction of the interchange criterion does not guarantee stability to ballooning at high  $\beta$ . However, FLR effects are expected to stabilize all but  $m = 1$  ballooning. Calculations for this mode in quadrupole-stabilized tandem mirror designs with close-fitting walls have yielded  $\beta$  limits remarkably close to limits found from the interchange criterion [10]. In addition, FLR should make the  $m = 1$  mode rigid, so that Ineq. (1) may in fact be pessimistic as a local condition on each field line.

We propose to furnish the additional pressure in the end cell with ECH electrons. These electrons must be able to respond to MHD instabilities in the center cell and not be "rigid" as in ring-stabilized devices. A simple criterion for MHD response of the electrons is  $\omega_d < \gamma_{MHD}$ , where  $\omega_d$  is the curvature drift frequency of the hot mantle electrons and  $\gamma_{MHD}$  is the growth rate of the instabilities in the center cell. Here the appropriate growth rate is that for  $m = 1$  instabilities of the center cell.

The mantle electrons must be axially confined by the magnetic field. If the mirror ratio for these electrons is small, their distribution function will be highly anisotropic leading to the possibility of enhanced losses due to anisotropy driven instabilities such as the whistler. As a guard against these instabilities, we specify a mirror ratio of at least two on the field lines threading the mantle electrons. For confinement of sloshing ions in the end cell a higher mirror ratio, around 3 or higher, is needed in the core. A magnet design for the end cell which satisfies these criteria is described in Section II. The mantle electrons must also follow closed drift surfaces satisfying the above-mentioned criterion on drift frequency. In the third section we present results on the electron drift and then consider heating of

these electrons. In the next section we evaluate radial transport of center-cell fuel ions, as caused by the octopole field. In the fifth and sixth sections we cover MHD stability and plasma parameters which can be expected in this configuration.

## II. MAGNET DESIGN

As described in the introduction, we wish to create a minimum- $|B|$  region external to the core plasma with octopole fields. All field lines passing through the minimum- $|B|$  region should have a mirror ratio of at least two to allow development of a sufficiently broad electron distribution function. In an initial attempt at meeting the above requirements, we chose the classic arrangement of Ioffe bars parallel to the  $z$ -axis with the mirror fields formed with circular coils. We found it difficult to obtain a mirror ratio of two on some mantle field lines near the outer mirror. This occurs because the field lines in this region, which are pulled outward by the Ioffe bars, experience a loss of mirror ratio due to cancellation of the mirror field by the Ioffe-bar field. To counteract this effect, it is necessary to bow the Ioffe bars outward much like the staves of a barrel.

An end-cell coil set including a barrel-shaped main octopole is shown in Fig. 3. Other elements in the coil set are a high-field (24 T) hybrid coil (i.e., superconducting coils with a small copper insert) similar to that proposed in the MARS design [8], a small octopole transition coil with bars parallel to the  $z$  axis, and a 7.5 T outer mirror coil. The octopole coils of Fig. 3a are only approximations to actual coils which would have smooth arcs



at junctions between the bars. This form was the only one possible with the coil generators available at the time this work reported here was performed. Recently, we have developed a generator for the coils shown in Fig. 3b which contains smooth arcs. Results for this shape are close to the coil set of Fig. 3a.

The bars of the main octopole coil are placed at  $\theta = 22.5, 67.5$ , etc. to the vertical (x) axis in Fig. 3. The  $\theta = 0, 45, 90$ , etc. planes are symmetry planes, i.e., have zero geodesic curvature. Contours of  $|B|$  at  $0, 22.5$  and  $45$  deg from the x-z plane, as obtained with the aid of the EFFI code [11], are shown in Figs. 4-6. Also shown are the trajectories of field lines which map to several center-cell radii. We note that the field lines in the  $45$  deg plane are most strongly radially deflected by the octopole field. For comparison we show in Fig. 7 the B-field contours and field lines for the  $\theta = 22.5$  deg plane for the same coils without the transition octopole and in Fig. 8 with no octopole field at all. The transition coil clearly aids in gathering field lines from the center cell so they pass through the outer mirror.

There is no unique prescription for adjusting the size and current in the transition coil. We chose the size quite arbitrarily, only desiring to keep it small and with adequate clearance between the coil and both the halo plasma and the mantle electrons. The transition-coil current was then adjusted to map the center-cell plasma surface into a circle at the midplane of the main end-cell octopole. Experience with quadrupole magnets has shown that this prescription assures closed, overlapping drift surfaces for barrier electrons, sloshing ions and passing center-cell ions. For currents near the chosen value, the surface deforms into the usual octopole shape. We found that small changes in the

transition-coil current and position could cause substantial changes in the shape of the flux surfaces in the end cell.

This coil would usually be constructed of superconductor, but since it need carry only about 1 MA in the present configuration, it could be constructed of copper and shaped more like the plasma surface. One such variation forms the coil on a cone with the small open end on the high-field side, as shown in Fig. 3b.

Figure 9 shows the contours of  $|B|$  in a quadrant of the x-y plane at the midplane of the main octopole. We see one of the four minima in  $|B|$  which occur in the octopole. Note that only a small radial well is formed - a mirror ratio of about 1.1 in this case. The hot mantle electrons fill the region with near constant pressure between the indicated surface of the core plasma and the minima. Pressure should rapidly decrease at radii beyond the minima.

For purposes of comparison with the MARS coils [8], we collect some parameters of interest in Table I. We see that the mirror-to-mirror length and total current have each been reduced over the values for MARS by a factor approaching three, while the volume of the superconductor and the stored energy are down by a factor of more than four. It should be noted that the volume does not include the choke coils which would be similar for the two reactors, nor does it include the coils used in MARS to recircularize the flux bundle for the direct converter. We expect that the latter coils, if needed, would also be smaller in the octopole configuration.

### III. PROPERTIES OF MANTLE ELECTRONS

The mantle electrons bridge the region between the core plasma in the end cell and the region of minimum  $|B|$ . Throughout this region they must drift on closed surfaces in order not to introduce a channel for losses of electrons. The average energy of the electrons should be chosen to minimize losses--high energies reduce scattering and drag losses but also increase synchrotron radiation. The energy for minimum loss rate depends on the density of background cold electrons. For our conditions, we find the minimum near 800 keV (Section V); in electron-ring stabilized devices, such as EBT or a fully axisymmetric tandem mirror, the cold electron density must be much higher and the minimum occurs near 1.5 MeV [12]. The mantle electrons must also satisfy the requirement  $\omega_d < \gamma_{MHD}$ .

Since the bounce frequency is much greater than the drift frequency, the electrons drift on surfaces of constant  $J$ . Although the electrons are relativistic, we compute the non-relativistic equations to obtain an initial idea of the shape of the surfaces [13],

$$J = \oint v_{||} ds \quad (2)$$

where  $v_{||}$  is the velocity component parallel to the magnetic field. Using the energy equation with no electrostatic potential, we rewrite Eq. (2) in the form

$$J = (2/m)^{1/2} \oint (\epsilon - \mu B)^{1/2} ds \quad (3)$$

where  $\epsilon$  is the total energy and  $\mu = m v_{\perp}^2 / 2 B$  is the magnetic moment. In general,  $J$  is a function of the field line coordinates, say  $r$  and  $\theta$ , at the midplane of the end cell,  $\mu$  and  $\epsilon$ . However, we are not interested in the magnitude of  $J$ , only in the shape of the constant- $J$  surfaces. We can, therefore, divide through by  $\epsilon$  and plot  $J$  surfaces as a function of  $r$  and  $\theta$  for various values of  $\mu/\epsilon$ . We choose to use  $R_e$ , the mirror ratio where the electrons reflect, in place of  $\mu/\epsilon$  as the independent variable.

The calculation of  $J$  has been carried out with the code GCDRIFT [14], which can also be used to compute the non-relativistic drift motion of ions and electrons in the vacuum magnetic field. The fields and their gradients are computed with filamentary approximations to the conductors.

We find that the constant- $J$  surfaces are nearly circular near the axis with small variations in radius of period  $4\theta$ , where  $\theta$  is the azimuthal angle. At increasing radii, the radial excursions grow in magnitude and the periodicity changes to  $8\theta$ . This behavior can be anticipated from considerations of the expansion of  $J$  near the axis for octopole fields which reads:

$$\begin{aligned} J(r, \theta, z, \mu/\epsilon) = & J_0(r, z) \\ & + r^4 \cos(4\theta) J_4(r=0, z, \mu/\epsilon) \\ & + r^8 \cos(8\theta) J_8(r=0, z, \mu/\epsilon) + \dots \end{aligned} \quad (4)$$

The  $8\theta$  azimuthal dependence is shown in the lower parts of Figs. 10 and 11 which display portions of the  $J$  surfaces for electrons reflecting at mirror ratios of 1.05 and 2.0. Since the field contains octal symmetry, only an octant of the surfaces is shown. In both figures we see axis-encircling  $J$

surfaces at both large and small radii, separated by islands which occur near the radius of the minimum IBI islands (compare Fig. 8). However, just outside the islands, the surfaces for  $R_e = 1.05$  maintain the 80 behavior while the next component, 160 becomes important for the surfaces for  $R_e = 2$ . The latter electrons sample fields closer to the octopole bars.

At first sight, it is surprising that the drift surfaces displayed in Figs. 10 and 11 contain one island per octant while the IBI contours in Fig. 9 display one per quadrant. Electrons drifting in a plane must drift parallel to the IBI contours since  $v_D B \times \text{grad } B$ , but the bounce motion samples different grad B so the J contours will, in general, deviate from the IBI contours at the midplane. As bounce motion is more limited axially, the J and IBI contours should approach. We have verified that the J islands do indeed coalesce into a single island per quadrant when mirror ratio = 1.01 electrons are considered.

For this stabilization scheme to be successful, the constant-pressure mantle electrons must extend to at least the minimum IBI location after which their density may fall to zero. We assume that they extend to about 1.05 m at  $\theta = 0$  where they are axis encircling. To determine the maximum electron energy for non-rigid behavior, we have computed the actual (non-relativistic) drift of 3.6 MeV electrons reflecting at  $R_e = 1.05$  and  $R_e = 2$ . The (non-relativistic) drift frequencies for these two cases are  $3.3 \times 10^5$  and  $1.4 \times 10^6$  rad/s, respectively. With the aid of the TEBASCO code [10,15], we found a growth rate for  $m = 1$  instabilities in the center cell of  $3.1 \times 10^5 \text{ s}^{-1}$  at an average  $\beta$  of 0.50. This is the same size as the curvature drift frequency for the bulk of the mantle electrons at  $R_e = 1.05$ . However, relativistic effects

increase the drift frequency by the factor  $\gamma$ , which is about 8 for 3.6 MeV electrons. From the criterion  $\omega_d < \gamma_{MHD}$ , we expect an upper limit of approximately 1 MeV for the energy of the mantle electrons.

Although we have not yet performed detailed calculations on electron-cyclotron heating of the mantle electrons, we have a general picture of how this might be accomplished. As previously discussed, the plug radial pressure profile should increase to a maximum at the minimum  $|B|$  point and then decrease beyond. As long as scattering dominates the hot-electron losses, minimizing the ECH power required to maintain the hot electrons requires maximizing the hot-electron energies, subject to the MHD constraints on their drift frequencies. At the peak pressure point (minimum  $|B|$  point), the curvature drifts change sign and so in the vicinity of this point the drift frequency does not constrain the energy, but rather synchrotron radiation places a soft limit around 1 MeV for ECH power minimization. The hot electron density is constrained only in the core, where density mapping to plug the central cell determines the barrier density. Thus we expect the radial density profile for the hot electrons to decrease monotonically with radius, while the pressure rises to the minimum  $|B|$  point.

The mantle electrons will therefore be at lower density and more relativistic than in the core (see Section V), and the ECH absorption efficiency for a single pass may be 10% or less in the mantle. We envision a set of mirrors arranged around the mantle so as to reflect a quasi-optical microwave beam for several passes through the mantle. Off-resonant frequencies can be used to control the hot-electron mantle  $\beta$  because absorption at relativistic energies is strongly Doppler- and mass-shifted. To control the mantle electron density,

a separate microwave beam aimed at an appropriate cold electron resonant zone intersecting the mantle can be used to control the lower energy electron population feeding the hotter anisotropic electrons. Since the mantle electrons are in a stable minimum  $|B|$  field, there is no hot electron interchange (Berk-Dominguez) mode requirement that the cold electron background density be dominant. We expect ECH feed requirements will allow the cold density to be much less than the hot density,  $n_{ec} \ll n_{eh}$ , the origin of the cold electrons being ionization of a low-pressure ( $< 10^{-6}$  Torr) gas background. Calculations using a Fokker-Planck code should be able to check this expectation.

### III. ION RADIAL TRANSPORT DUE TO DRIFTS

In order to avoid excessive losses due to radial transport of center-cell ions in MARS, it was necessary to cancel deflections of passing ions (i.e., those center-cell ions which pass into the end cell) by adding C coils to symmetrize the geodesic curvature in the end cell. To obtain a short end cell, such added coils must be avoided. In this section we estimate the confinement time of center-cell ions with an octopole end cell. For this estimate we use the fastest diffusion coefficient due to classical processes, namely that for stochastic or plateau diffusion,

$$D = a^2 / (4 \tau_b R) \quad (5)$$

where  $a$  is the maximum deflection of an ion on a single reflection from the end cell as measured in the center cell,  $\tau_b$  is the bounce time for a complete

cycle, and  $R$  is the central-cell mirror ratio for the ions, in this case 24/3.3. The mirror ratio factor occurs in Eq. (5) because  $\sim 1-1/2R$  of the ions are reflected by the large mirror field and do not see the octopole fields.

If the paraxial approximation to the magnetic fields is applicable, the radial deflection of a passing ion on a single reflection in the end cell will obey the relation

$$\delta r = a \cos (4 \theta) \quad (6)$$

and the amplitude,  $a$ , will scale as  $r^3$ . In order to verify that this relation is valid and to ascertain the value of  $a$ , we have computed deflections with the aid of the GCDRIFT code [14]. Ions were started with various pitch angles in the axisymmetric region of the central cell, reflected elastically by a wall at the approximate location of the axial confining potential (see Fig. 1) and then followed back to the  $z$  location of their starting point. The difference in radial position is then the deflection  $\delta r$ . As for the electron drifts reported in Section II, only vacuum fields with no electrostatic potentials were used.

It was found that  $\delta r$  was very nearly independent of the initial pitch angle if the pitch angle was small enough for the ions to pass through the choke coil. Consequently, we used only a single pitch angle near the loss cone for this study. The amplitude,  $a$ , of the deflection was computed for several values of initial radius in the center cell between .1 m and the plasma edge at .45 m and azimuthal angles from 0 to  $90^\circ$ . Fig. 12 shows that  $\delta r$  follows closely the sinusoidal function given in Eq. (6) with some distortion at large



r. The deflection is given vs. radius in Fig. 13. Also shown for comparison is the deflection as computed without a transition coil. We see that the deflection does scale as  $r^3$  as expected and that the addition of the transition coil substantially reduces the deflection. The transition coil also makes the field more paraxial in nature as demonstrated by closer agreement with  $r^3$  scaling.

We can define a radial confinement time,  $t_r$ , at any radius by

$$t_r = \frac{L}{2\pi r D} \frac{\int n(r) r dr}{\int n(r) r dr} \quad (7)$$

where  $n$  is the ion density. For a quartic density profile, which we use to model reactors, Eq. (7) becomes

$$t_r = (r_p^4 / 8r^2 D) [1 - (1/3) (r/r_p)^4] \quad (8)$$

where  $r_p$  is the core plasma radius. Diffusion coefficients and confinement times are given in Table II. We see that the confinement time is high, even at the outer edge of the plasma. For comparison, it should be noted that center-cell ions trap in the end cell with a characteristic time of 1 s. Thus, radial transport should be of no concern in octopole-stabilized end cells and there is no need for additional coils to cancel the radial deflection.

We can gain additional insight into the radial transport from considerations of the geodesic curvature. In analyzing quadrupole-stabilized tandem mirrors, it has been found convenient to form normal and geodesic components of the field line curvature

$$\kappa = R \text{ grad } \psi + R \text{ grad } \theta \quad (9)$$

with  $\mathcal{R}$  the normal curvature and  $\mathcal{H}$  the geodesic curvature.  $\psi$  and  $\theta$ , the magnetic flux and angular position of a field line in the center cell, where flux surfaces are circular, are the generalized field-line coordinates. The deflection of a passing ion in one reflection in the end cell can be written

$$\delta \psi = 2(m/q) \int_0^{s_t} \mathcal{H} (v_{\parallel} + v^2/2v_{\parallel}) ds \quad (10)$$

where  $s_t$  is the location of the turning point. Only ions with  $v_{\parallel} \gg v_{\perp}$  are able to make it through the choke coil so the quantity in parentheses is nearly constant. Thus, the radial deflection is approximately proportional to an integral of a field property along the field line.

The quantities  $\mathcal{H}/r_0^2$  and  $\int (\mathcal{H}/r_0^2) ds$  are plotted for the field line at  $22.5^\circ$  in Figs. 14 and 15. Values are shown both with and without the transition octopole. Comparing the curves in Fig. 14, we see that the addition of the transition magnet has (1) introduced a new region of positive  $\mathcal{H}$ , (2) reduced the magnitude of  $\mathcal{H}$  near its maximum by a factor of about four, and (3) rendered the maximum and minimum curvature almost symmetric about the midplane of the main octopole. As a result, the integral, shown in Fig. 15, is reduced by a factor of about 15. If so desired, we could reduce the integral to zero by adjustment of the transition current and/or position. Such adjustments would then probably cause the flux tube from the center cell to be non-circular at the midplane of the end cell.

#### IV. MHD STABILITY

A full computational capability for the MHD stability of the octopole configuration is currently under development. As described in the introduction, probably only  $m = 1$  modes are of concern, and, when a close-fitting wall is present, as it is in a reactor, ballooning may be suppressed and the mode becomes flute-like. We can at least show here that this octopole configuration can meet the classical low- $\beta$  interchange stability condition of Ineq. (1). In a study of the multipole effects on the flux surfaces, Kaiser et al. [16] have recently shown that there is little octopole dependence of the interchange criterion in the plasma core. We apply this relation to the core plasma to obtain the required increment in hot-electron pressure at the edge of the core. We assume that maintenance of this pressure out to the minimum- $|B|$  region will serve to stabilize the entire machine.

To apply Ineq. (1) to the octopole, we need to specify a pressure function. We choose  $p$  to be separable in  $\psi$  and  $B$ ,

$$p = \omega(\psi) p(B) \quad (11)$$

For the core plasma we use a quartic profile in radius,

$$\omega = 1 - (\psi/\psi_p)^2 \quad (12)$$

and for the extra hot electrons in the end-cell core which are needed to stabilize the core,

$$\omega = (\psi/\psi_p)^2 \quad (13)$$

where  $\psi_p$  is the magnetic flux at the core plasma surface.

For the pressure function,  $p = p_{||} + p_{\perp}$ , in the core, we use the following model functions [15]:

Center-Cell Ions ( $0 < z < z_{m1}$ )

$$\hat{p}_{||} = \hat{p}_{\perp} = \frac{1}{2} \beta_c B_c^2 \quad (14)$$

Passing Ions ( $z_{m1} < z < z_b$ )

$$\hat{p}_{||} = \frac{1}{2} \beta_c B_c^2 \frac{1}{4} \left[ 5 \frac{B}{B_{m1}} - \left( \frac{B}{B_{m1}} \right)^5 \right] \quad (15)$$

$$\hat{p}_{\perp} = \frac{1}{2} \beta_c B_c^2 \left( \frac{B}{B_{m1}} \right)^5 \quad (16)$$

Passing Ions ( $z_b < z < z_{m2}$ )

$$\hat{p}_{||} = \frac{1}{2} \beta_c B_c^2 \left[ \frac{5}{4} \frac{B_b}{B_{m1}} - \frac{1}{4} \left( \frac{B_b}{B_{m1}} \right)^5 \right] \left( \frac{B}{B_b} \right)^{1+\delta} \left( \frac{B_{m2} - B}{B_{m2} - B_b} \right)^2 \quad (17)$$

$$\hat{p}_{\perp} = \left( \frac{2B}{B_{m2} - B} - \delta \right) \hat{p}_{||} \quad (18)$$

$$\delta = \frac{2B_b}{B_{m2} - B_b} + \frac{4B_b^4}{B_b^4 - 5B_{m1}^4} \quad (19)$$

Sloshing Ions and Hot Electrons ( $z_{m1} < z < z_{m2}$ )

$$\hat{p}_{||} = \frac{1}{2} \beta_b B_b^2 \frac{(B_{m2} - B)^2}{B_{m2}^2 - B_b^2} \quad (20)$$

$$\hat{p}_{\perp} = \frac{1}{2} \beta_b B_b^2 \frac{B_{m2}^2 - B^2}{B_{m2}^2 - B_b^2} \quad (21)$$

$$\hat{p}_{||} = p_{\perp} = 0, \quad B > B_{m2} \quad (22)$$

$\beta_c$  and  $\beta_b$  are input values for the plasma properties, and  $B_c$ ,  $B_{m1}$ ,  $B_b$ , and  $B_{m2}$  are magnetic fields at key locations (see Fig. 1).

The "extra" stabilizing hot electrons in the core are expected to be narrower in axial extent than the combination of hot electrons and sloshing ions represented by Eqs. (20)-(22). We use the same pressure functions as in Eqs. (20)-(22) but with the replacement of  $\beta_b$  by  $\beta_m$  and  $B_{m2}$  by  $B_{max}$ , where the mirror ratio  $B_{max}/B_b$  is chosen to be two.

We can now substitute Eqs. (11)-(22) in Ineq. (1) and solve for the minimum  $\beta_m$  as a function of  $\beta_c$  and  $\beta_b$ . Results are displayed in Fig. 16. The stability criterion is linear in  $\beta$  and we can fit it with the function

$$\beta_m = 1.2 \beta_b + 0.56 \beta_c \quad (23)$$

Typical reactor parameters are  $\beta_c = .75$ ,  $\beta_b = .30$  for which the mantle electrons must have  $\beta_m = .78$ . Note that this is the total  $\beta$  at the edge of the plasma (based on the center-line vacuum field), so the increase in  $\beta$

from the center line to the edge is  $.78 - .30 = .48$ . This plasma pressure is assumed constant out to the edge of the mantle electrons.

The above analysis is based on the interchange relation while we expect  $m = 1$  ballooning to set the limit on stability. The  $m = 1$  ballooning is a rigid-body type of motion and stabilization comes from a  $\psi$  (radial) average of the forces [10]. It is possible that the ballooning analysis, which is currently under development [16], will allow radial profiles of mantle pressure which are not monotonically increasing. In other words,  $p_m$  could actually decrease from the core to just inside the region of minimum  $|B|$  and then increase to a high electron pressure which would prevent rigid motion of the plasma column.

An additional stabilizing mechanism not explicitly included here arises from the presence of conducting walls near the edge of the plasma. If the center-cell average  $\beta$  is high enough, of order 0.90, the image currents in the wall will stabilize against  $m = 1$  ballooning [17]. If the center-cell is fully stabilized in this way, then, by Eq. (23),  $\beta_m$  need be only some 20% higher than  $\beta_b$ . Even if the wall stabilization is only partially effective, it could reduce  $\beta_m$  below the value found from Eq. (23).

## V. PLASMA PARAMETERS

In order to compute the power flow for a reactor application of this scheme, we form point-model equations for the densities and energies of the various plasma components. Components considered are center-cell composite D-T ions, alpha particles and electrons, sloshing ions (injected at point  $a'$  in

Fig. 1), trapped ions in the end cell, the warm, potential-forming electrons (near point a), and the hot barrier electrons (near point b). In addition, the potential is computed at cardinal points. The thermal barrier plug models employed are essentially those given in Refs. 8 and 18, with some changes and additions described below.

The reactor is assumed to operate in a well-plugged mode, i.e., the axial losses of center-cell ions are small compared to the losses due to trapping in the end cell. In this way, alpha particles are removed from the center cell by this trapping process and no pumping in the center cell is needed. The alpha particles and fuel ions which trap in the end cell must then be removed by a pump. Earlier concepts as well as current experiments employ charge-exchange pumping with a neutral beam. This form of pumping requires considerable power input and has been discarded in reactor designs in favor of some form of induced radial loss called drift-pumping. Drift-pumping in the quadrupole plugs of the MARS design [8] exploited the large geodesic curvature of field lines near the mirrors to enhance radial drifts due to small magnetic perturbations at the trapped ion bounce frequencies. Due to near axisymmetry in the octopole design, the equilibrium field line curvatures are much smaller than in the MARS quadrupole design, thus requiring much stronger magnetic perturbations applied to pump trapped ions in the octopole plug compared to MARS. We have not yet found a solution to drift-pumping in an octopole-stabilized plug design. However, we are currently investigating various ways to induce azimuthal electrostatic perturbations at trapped ion bounce frequencies to accomplish the necessary radial transport, and some appear promising. One approach would be to apply higher frequency RF waves (ICRF or lower hybrid)

to induce electron Landau damping and associated electrostatic fields, and the amplitude-modulate the HF waves at the trapped ion drift or bounce frequencies. Another approach would be to segment the direct converter plates at the end walls and superimpose appropriate AC voltages which would propagate azimuthal electric fields down the field lines to the plugs. For the present paper, we can only show that the magnetic geometry of the octopole design we propose is compatible with reasonable plasma power balance, assuming that the power consumption required for drift-pumping can be small. Thus in what follows, we estimate other plug plasma power requirements for an octopole design.

We consider now the computation of the power for heating the hot electrons in the end cell. Power to the electrons is required to make up for losses due to Coulomb collisions and radiation. Shearer [19] has developed expressions for power losses (MW) due to: (1) scattering off hot electrons and the neutralizing ions; (2) drag on cold electrons; and (3) scattering off cold electrons and their neutralizing ions, which can be put in the form:

$$P_1 = \frac{10^{-3} \text{ eV } C_h^{(2)} A_h^{(2)} n_{eh}^2 \gamma [2/(\gamma + 1)]^{3/2} (E_h/2)}{2.4 \times 10^8 E_{eh}^{3/2} \log R_b} \quad (24)$$

$$P_2 = \frac{10^{-3} \text{ eV } C_{hc}^{(2)} A_{hc}^{(2)} n_{eh} n_{ec} \gamma [2/(\gamma + 1)]^{1/2} (E_h - 3T_{ec}/2)}{8.3 \times 10^7 E_{eh}^{3/2}} \quad (25)$$

$$P_3 = \frac{10^{-3} \text{ eV } C_{hc}^{(2)} A_{hc}^{(2)} n_{eh} n_{ec} \gamma [2/(\gamma + 1)]^{3/2} (E_{eh}/2)}{2.0 \times 10^8 E_{eh}^{3/2} \log R_b} \quad (26)$$



where  $E_{eh}$  is the hot electron energy (keV),  $n_{eh}$  is their density ( $\text{cm}^3$ ),  $n_{ec}$  is the density and  $T_{ec}$  the temperature of the cold electrons,  $V$  is the volume of the region in question,  $R_b$  is the mirror ratio for the hot electrons, and  $C^{(2)}$  and  $A^{(2)}$  are weighting factors for the averages of the density products over the radial and axial profiles. For the purpose of this analysis, the hot-electron average energy is assumed constant in three regions: core, halo (between the core and the flux tube just clearing the inner edge of the choke coil), and the (outer) mantle (from the halo to just beyond the minimum  $|B|$  region). In reality, we would like to supply ECH so that the hot-electron energy rises from the center line to a peak in the minimum  $|B|$  region, as described in Section II. Such a profile should lower electron losses due to scattering below the values computed in this section, since the average density would be lower.

We take the density to be a separable function of radius and axial position,  $n = n(r)f(z)$ . A typical radial factor is then

$$C_h^{(2)} = \frac{2}{r_b^2} \int_0^{r_b} \left[ \frac{n_{eh}(r)}{n_{ehb}} \right]^2 r \, dr \quad (27)$$

and an axial factor

$$A_h^{(2)} = \frac{1}{L_b} \int_0^{L_b} f^2(z) (B_b/B) \, dz \quad (28)$$

where the factor  $B_b/B$  accounts for the variation of flux-tube area along the axis,  $B_b$  being the plasma-reduced magnetic field at point  $b$ .

The loss of power through synchrotron radiation can be written in the form [20]:

$$P_s = 3.9 \times 10^{-4} \text{ eV } C^{(s)} A^{(s)} n_{eh} B^2 E_{eh} [1 + 2.5 (\gamma - 1) + 1.5 (\gamma - 1) / (\gamma - 0.3)] \quad (29)$$

$C^{(s)}$  and  $A^{(s)}$  are radial and axial averages of  $n_{eh} B^2$  over radius and axial position as in Eqs. (27) and (28). Equation (29) has been derived [20] for electrons with a Maxwellian distribution of velocities. Because the high-energy electrons will lose energy by radiation more rapidly than the low-energy electrons, we would expect the tail population to be depressed below that for a Maxwellian distribution and Eq. (29) to overestimate the losses.

As described above, we divide the end-cell into three regions: core, halo, and mantle. The core cold-electron density is assumed quartic in radius, as in Eq. (12), while the hot electron density is the sum of the two profiles in Eq. (12) and (13). The core volume (both ends) is given by

$$V_b = 2\pi r_c^2 L_b B_{cv} \sqrt{1 - \langle \beta_c \rangle / B_{bv}} \sqrt{1 - \langle \beta_b \rangle} \quad (30)$$

where  $r_c$  is the center-cell radius and subscript v denotes the vacuum field.

The radial factors are found to be

$$C_h^{(2)} = 1 + \frac{2\Delta n_{eh}}{3n_{ehb}} - \frac{1}{5} \left( \frac{\Delta n_{eh}}{n_{ehb}} \right)^2 \quad (31)$$

$$C_{hc}^{(2)} = \frac{2 (1 + \Delta n_{eh}/n_{ehb})}{15} \quad (32)$$

$$C^{(s)} = 1 + \frac{\Delta n_{eh}}{3n_{ehb}} - \frac{2\Delta \beta}{15(1 - \beta_b)} \quad (33)$$

where  $\Delta n_{eh} = \beta_m B_{bv}^2 / 1.6 E_{eh} - n_{ehb}$  and  $\Delta \beta_b = \beta_m - \beta_b$ . To compute the axial factors in the core we take a hot electron density distribution corresponding to the pressure distribution in Eqs. (20) and (21),

$$n_{eh} = \frac{\beta_b B_b^2}{1.6 E_{ehb}} \left( \frac{3B_{max} + B}{3B_{max} + B_b} \right) \left( \frac{B_{max} - B}{B_{max} - B_b} \right) \quad (\text{Core}) \quad (34)$$

For the cold density we use a Gaussian function inboard of the barrier point  $b$  (Fig. 1),

$$n_{ec} = n_{ecb} \exp \left[ - (z - z_{m1})^2 / \ell^2 \right] \quad (35)$$

with  $\ell^2 = (z_b - z_{m1})^2 \ell n[n_{ec}(z_{m1})/n_{ecb}]$  and a constant outboard of the barrier.

The axial factors become

$$A_h^{(2)} = 0.19 \quad (36)$$

$$A_{hc}^{(2)} = 0.78 \quad (37)$$

$$A^{(s)} = 0.31 \quad (38)$$

The halo contains cold electrons of about  $10^{12} \text{ cm}^{-3}$  density and 50 eV energy [8]. This plasma streams out from the center cell through the end-cell to collectors in the end tanks. We assume constant cold-electron density with hot electron density constant vs. radius, but following a more-sharply peaked axial profile:

$$n_h = \frac{\beta B_b^4}{1.6 E_{eh} B^2} \left( \frac{B_{max} - B}{B_{max} - B_b} \right)^{5/2} \quad (\text{Halo}) \quad (39)$$

We expect stronger axial peaking in this region because of the lower collision frequency and applied ECH. We take the electron energy to be

constant, typically 500 keV and compute the required power. Radial factors are unity for this case while the axial factors become

$$A_h^{(2)} = 0.12 \quad (40)$$

$$A_{hc}^{(2)} = 0.38 \quad (41)$$

$$A^{(s)} = 0.18 \quad (42)$$

The halo volume (both ends) is

$$V_h = 2\pi[r_{ch}^2 - (r_{ch} - \delta r_{ch})^2] (B_m/B_{bv})L_b \quad (43)$$

with  $r_{ch}$  the inner radius of the choke coil (ml in Fig. 3) and  $\delta r_{ch}$  the clearance between the choke coil and the core plasma. The hot-electron density follows from the requirement of constant pressure,

$$n_{ehh} = (\delta n_{eh} + n_{ehb})E_{ehb}/E_{ehh} \quad (44)$$

The mantle region is treated in the same way as the halo but the mantle hot electron energy is assumed higher, ca. 800 keV and cold density lower, ca.  $10^{11} \text{ cm}^{-3}$ .

In order to compute the plasma properties, we need to specify the injection energy of the sloshing ions. The maximum energy is limited by the requirement that the ions remain adiabatically confined. To estimate the adiabatic energy limit, we can use the formula [21]

$$E_{ad} \text{ (keV)} = \frac{10^3 \kappa^2 B_{min}^2 L_{||}^2 Z_i^2}{M_i (1 - 0.036 \ln \Lambda)^2} \quad (45)$$

where  $B_{min}$  is the minimum magnetic field,  $Z_i e$  and  $M_i$  are the charge and mass (AMU) of the ion,  $L_{||} = (2B/\partial^2 B/\partial s^2)^{1/2}$  is the scale length for a parabolic well at the minimum, and  $\Lambda$ , which is a function of  $E$ , and  $\kappa$  are defined in Ref. 19.

Evaluating the parameters for the vacuum field we find  $L_{||v} = 1.77$  m and  $E_{adv} = 1.1$  MeV. Both  $B$  and  $L_{||}$  are reduced when the plasma is present. We can use the long-thin approximation,  $B^2 = B_v^2 - 2p_{\perp}$  ( $B$ ) together with Eq. (21) to find both  $B$  and  $L_{||}$ . For a peak  $\beta_b$  of .30 we find  $L_{||} = 1.47$  m and  $E_{ad} = 600$  keV. Since this is the ion energy measured at the midplane, the injection energy must be about 100 keV less to allow for the difference in the potential between the injection point (a' in Fig. 1) and the end-cell midplane. We have taken 475 keV for the calculations.

Properties have been computed for two cases representative of small reactors: one with a 50 m long center cell producing about 500 MW of fusion power and one twice as long producing about 1000 MW. Center and end-cell peak  $\beta$ 's were fixed at 75% and 30% respectively. From the results of Section IV, we see that we must have  $\beta_m = 78\%$  for stability. As indicated in Table IV, certain other properties such as the center-cell ion temperature, and cold-electron density and hot-electron energy in the mantle were fixed. The power flow for these two examples is given in Table III and a selection of the plasma properties in Table IV.

When considering these results we should note that only a limited attempt was made to optimize the parameters. The center-cell size,  $\beta$ , vacuum field

and temperature were chosen to give the desired total fusion power.  $\beta_b$  was chosen to yield a moderate value of  $\beta_m$  and the mantle hot-electron energy was chosen at the approximate minimum in the mantle ECH requirements, i.e., where the scattering losses were about the same as the synchrotron radiation. Larger Q values could doubtless be obtained by a more optimum choice of parameters.

For the 500 MW reactor, the Q value of 10 indicates that there would be a substantial recirculating power fraction, while at 1000 MW the Q is essentially the same as computed for the much larger MARS reactor. Since the end-cell size is fixed, it is rather surprising that the Q isn't simply doubled on going to the larger power. In comparing the two cases, we see that the power to the core electrons has decreased from 28.9 to 17.6 MW in increasing the center-cell length. This results from two constraints on the solution: (1)  $\beta_b = 0.30$ , and (2) trapping rate of alpha particles in the end-cell = rate of formation of thermal alphas. To satisfy the latter condition, the trapped density in the barrier is adjusted. Higher trapping rates are obtained at lower trapped-ion density because of higher gradients across the passing-trapped separatrix in velocity space. Because of the lower density at the barrier, the hot-electron density is lower, and the first constraint allows higher hot-electron energy, thus reducing the scattering rate and the power required. It may also be noted in Table IV that the thermal alpha concentration is higher in the center cell at higher power which also increases the trapping rate.

## VI. DISCUSSION

We have seen that the octopole stabilizing scheme allows considerable reduction of the end-cell length, thus allowing the design of high-Q tandem mirror reactors at much lower fusion power than previously thought possible. The results indicate that one could obtain  $Q > 20$  at a power of about 1000 MW. The short end cell (7.7 m) coupled with short modules for the center cell ( $< 10$  m) suggest that this reactor could be built in a factory, and then assembled on site, thus reducing construction costs over conventional on-site construction.

Although we have presented estimates and discussions of most physics problems, there are several areas which will require a much more detailed study. A principal area concern is the required  $\beta$  of the mantle electrons. This can only be resolved when codes are developed to analyze the stability of the entire system, particularly for  $m = 1$  modes in the presence of conducting walls. Also, the preferred electron energy profile rises from the minimum on axis to a maximum of about 800 keV at the minimum  $|B|$  location. Questions on the feed of cold electrons to the hot electron population, the required ECH frequencies and the wave propagation need to be addressed.

REFERENCES

- [1] DIMOV, G.I., ZAKAIDAKOV, V.V., KISHINEVESKY, M.E., Fiz. Plasmy 2, (1976) 597.
- [2] FOWLER, T.K., LOGAN, B.G., Comments Plasma Phys. Controlled Fusion 2, (1977) 167.
- [3] LOGAN, B.G., BARR, W.L., BENDER, D.J., CARLSON, G.A., et al., Plasma Physics and Controlled Nuclear Fusion Research 1978, Vol. 3, (IAEA, Vienna, 1983) 401.
- [4] BALDWIN, D.E., LOGAN, B.G., Phys. Rev. Lett. 43, (1979) 1318.
- [5] KESNER, J., Nuclear Fusion 20, (1980) 557.
- [6] BERK, H.L., ROSENBLUTH, M.N., WONG, H.V., ANTONSEN, T.M., BALDWIN, D.E., LANE, B., Plasma Physics and Controlled Nuclear Fusion Research 1982, 2, (IAEA, Vienna, 1983) 175.
- [7] KESNER, J., POST, R.S., MCVEY, B.D., SMITH, D.K., Nucl. Fusion 22, (1982) 549.
- [8] LOGAN, B.G., et al., "MARS-Mirror Advanced Reactor Study," Lawrence Livermore National Laboratory, Livermore, CA, Report UCRL-53480 (1984).
- [9] LOGAN, B.G., Comments Plasma Phys. and Controlled Fusion 8, (1984) 85.
- [10] KAISER, T.B., NEVINS, W.M., PEARLSTEIN, L.D., Phys. Fluids 26, (1983) 351.
- [11] SACKETT, S.J., Lawrence Livermore National Laboratory, Livermore, CA, Report UCRL-52402 (1978).
- [12] UCKAN, N.A., Phys. Fluids 25, (1982) 2381.



- [13] NORTHROP, T.J., The Adiabatic Motion of Charged Particles, Interscience Publishers (1963).
- [14] DEVOTO, R.S., "GCDRIFT-A Code for Following Guiding-Center Trajectories in Magnetic and Electric Fields," unpublished.
- [15] PEARLSTEIN, L.D., KAISER, T.B., LODESTRO, L.L., MARON, N., NEVINS, W.M., WILLMAN, P.A., Lawrence Livermore National Laboratory, Livermore, CA, Report UCID-19869 (1984).
- [16] KAISER, T.B., NEWCOMB, W.A., PEARLSTEIN, L.D. (submitted for publication).
- [17] KAISER, T.B., PEARLSTEIN, L.D., submitted to Phys. Fluids; KAISER, T.B., LODESTRO, L.L., PEARLSTEIN, L.D., Bulletin APS 29, (1984) 1300.
- [18] CAMPBELL, R.B., Lawrence Livermore National Laboratory, Livermore, CA, Report UCID-19875 (1983).
- [19] SHEARER, J.W., Lawrence Livermore National Laboratory, Livermore, CA, Report UCID-19577 (1982).
- [20] UCKAN, T., UCKAN, N.A., Phys. Fluids 25, (1982) 2372.
- [21] COHEN, R.H., ROWLANDS, G., FOOTE, J.H., Phys. Fluids 21, (1978) 627.

TABLE I. COMPARISON OF MARS [8] AND OCTOPOLE END CELL COILS. CHOKE AND RECIRCULARIZATION COILS FOR THE DIRECT CONVERTER ARE NOT INCLUDED.

	<u>MARS</u>	<u>Octopole</u>
Mirror to mirror length-m	21.8	7.7
Total current-MA	70.6	25.2
Conductor volume-m <sup>3</sup>	87.3	19.8
Stored energy-GJ	6	1.4

TABLE II. RADIAL DIFFUSION COEFFICIENTS AND CONFINEMENT TIMES AT SEVERAL CENTER-CELL RADII.

<u>r-m</u>	<u>D-m<sup>2</sup>/s</u>	<u>t<sub>r</sub>-s</u>
0.10	0.019	4.8x10 <sup>6</sup>
0.20	1.2	7.2x10 <sup>4</sup>
0.30	26	1900
0.40	215	117
0.45	561	27

TABLE III. POWER FLOW FOR TWO OCTOPOLE TANDEM MIRROR REACTORS WITH NOMINAL FUSION POWERS OF 500 AND 1000 MW.

---

Total fusion power-MW	520	990
Wall neutron power-MW/m <sup>2</sup>	2.2	2.0
at wall radius-m	0.61	0.61
End-cell power absorbed:		
Neutral beam (475 keV)-MW	0.39	0.42
ECH at a-MW	0.66	0.52
Core ECH at b-MW	28.9	17.6
Mantle ECH in halo-MW	7.5	7.5
Mantle ECH in mantle-MW	13.3	13.3
Total power absorbed-MW	51	36
Q	10	25

---

TABLE IV. PLASMA PROPERTIES FOR TWO OCTOPOLE TANDEM MIRROR REACTORS WITH NOMINAL FUSION POWER OF 500 AND 1000 MW. PROPERTIES MARKED WITH AN ASTERISK ARE INPUT QUANTITIES.

Center Cell:

Length*-m	50	100
Radius*-m	0.45	0.45
Vacuum magnetic field*-T	3.3	3.3
Peak $\beta^*$	0.75	0.75
Ion temperature*-keV	40	40
Electron temperature-keV	27	27
Ion Density- $10^{14} \text{ cm}^{-3}$	2.3	2.3
Thermal alpha concentration	0.035	0.048
$n \tau$ - $10^{14} \text{ s-cm}^{-3}$	5.3	5.6
D-T fueling current-A	340	610

End Cell:

Length*-m	7.7	7.7
Radius*-m	0.59	0.59
Vacuum field*-T	1.5	1.5
Peak $\beta^*$	0.30	0.30
Hot electron energies-keV		
Core	213	280
Halo*	500	500
Mantle*	800	800
Hot electron densities- $10^{12} \text{ cm}^{-3}$		
Core	7.0	5.7
Halo	11	11
Mantle	6.8	6.8
Cold electron densities- $10^{12} \text{ cm}^{-3}$		
Core	0.22	0.18
Halo*	1.0	1.0
Mantle*	0.10	0.10

# FIGURE CAPTIONS

Fig. 1. Magnitude of the magnetic field,  $B$ , and electrostatic potential,  $\phi$ , along the  $z$  axis.

Fig. 2. Magnitude of the magnetic field,  $B$ , and plasma pressure,  $p$ , vs. radial coordinate  $\psi = r_0^2 B/2$  at the midplane of the center cell (top) and end cell (bottom).

Fig. 3a. View of the end-cell magnets showing the hybrid mirror coil ( $m1$ ), the octopole transition coil ( $o1$ ), the main octopole coil ( $o2$ ), and the outer mirror coil ( $m2$ ).

Fig. 3b. Same as Fig. 3a but with conical transition magnet and continuously wound octopole.

Fig. 4. Contour plot of magnetic field in the  $\theta = 0$  deg plane in the end cell showing trajectories of field lines starting in the center cell at various radii. 1:  $r_0 = 0.15$  m, 2:  $r_0 = 0.30$  m, 3:  $r_0 = 0.45$  m (plasma edge), 4:  $r_0 = 0.61$  (wall), 5:  $r_0 = 0.67$  m.

Fig. 5. Contour plot of magnetic field in the  $\theta = 22.5$  deg plane in the end cell showing trajectories of field lines starting in the center cell at various radii. 1:  $r_0 = 0.15$  m, 2:  $r_0 = 0.30$  m, 3:  $r_0 = 0.45$  m (plasma edge), 4:  $r_0 = 0.61$  (wall), 5:  $r_0 = 0.67$  m.

Fig. 6. Contour plot of magnetic field in the  $\theta = 45$  deg plane in the end cell showing trajectories of field lines starting in the center cell at various radii. 1:  $r_0 = 0.15$  m, 2:  $r_0 = 0.30$  m, 3:  $r_0 = 0.45$  m (plasma edge), 4:  $r_0 = 0.61$  (wall), 5:  $r_0 = 0.67$  m.

Fig. 7. Contour plot of magnetic field in the  $\theta = 22.5$  deg plane in the end cell without a transition coil showing trajectories of field lines starting in the center cell at various radii. 1:  $r_0 = 0.15$  m, 2:  $r_0 = 0.30$  m, 3:  $r_0 = 0.45$  m (plasma edge), 4:  $r_0 = 0.61$  (wall), 5:  $r_0 = 0.67$  m.

Fig. 8. Contour plot of magnetic field in the plane perpendicular to the z axis in the end cell without octopole coils. Also shown are trajectories of field lines starting in the center cell at various radii. 1:  $r_0 = 0.15$  m, 2:  $r_0 = 0.30$  m, 3:  $r_0 = 0.45$  m (plasma edge), 4:  $r_0 = 0.61$  (wall), 5:  $r_0 = 0.67$  m.

Fig. 9. Contour plot of magnetic field in the x-y plane at the midplane of the main octopole.

Fig. 10. Portion of the J surface for mantle electrons reflecting at  $R = 1.05$ .

Fig. 11. Portion of the J surface for mantle electrons reflecting at  $R = 2$ .

Fig. 12. Radial deflection of passing ions vs. azimuthal angle for initial radii of .3, .4 and .45 m.

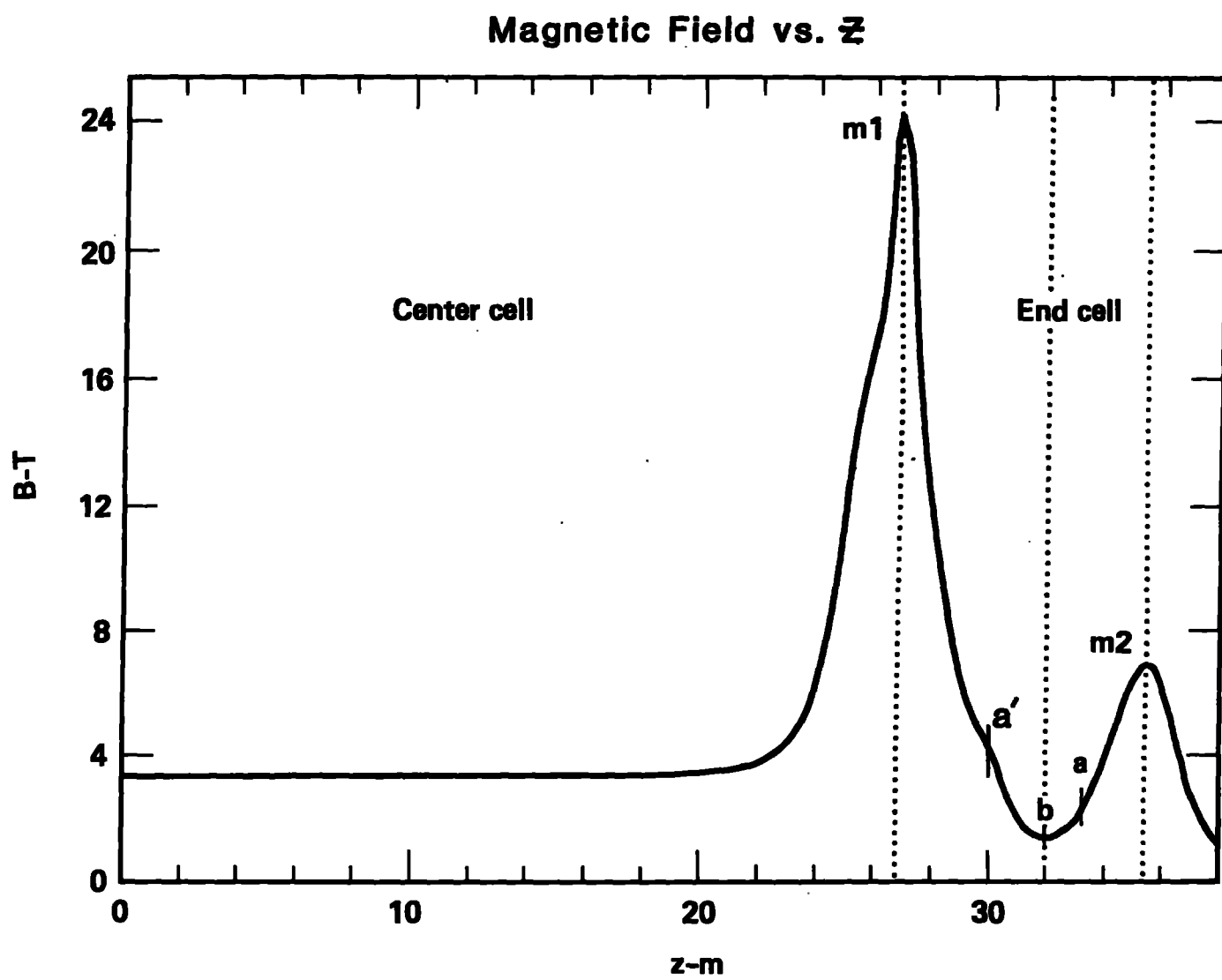
Fig. 13. Amplitude of the radial deflection of passing ions vs. initial radius with \_\_\_\_\_ and without ---- transition octopole coil.

Fig. 14. Geodesic curvature,  $\kappa$ , vs.  $z$  for a field line starting at  $r_0 = .45$  m and  $\theta = 22.5^\circ$  in the center cell. — : with transition octopole; --- : without transition octopole.

Fig. 15.  $\int_0^z (\kappa/r_0^2) ds$  vs.  $z$  for a field line starting at  $r_0 = .45$  m and  $\theta = 22.5^\circ$  in the center cell. — : with transition octopole; --- : without transition octopole.

Fig. 16. Mantle  $\beta_m$  required to stabilize octopole tandem mirror with peak center-cell  $\beta_c$  and peak barrier  $\beta_b$ .

Figure 1a





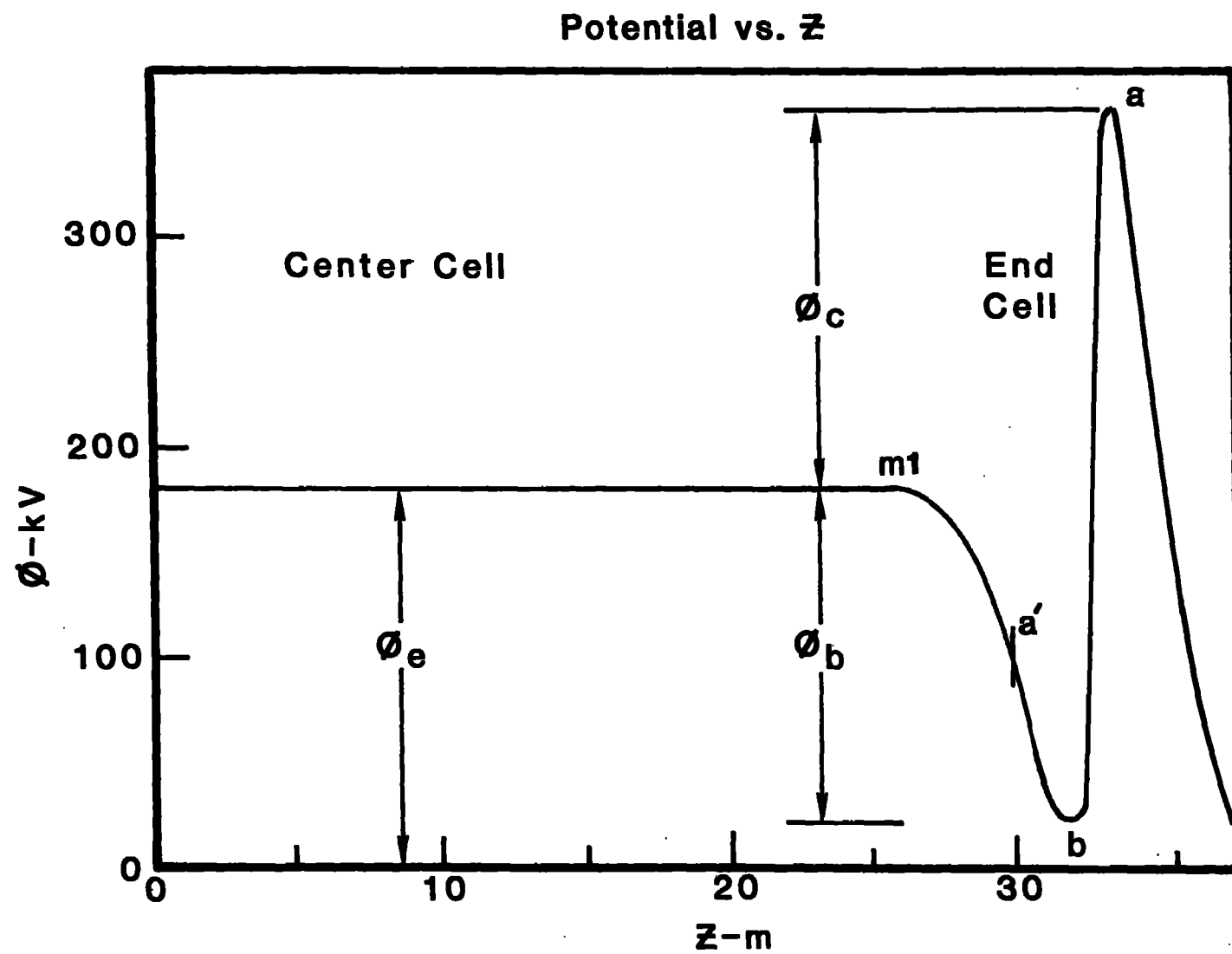


Figure 1b

Figure 2

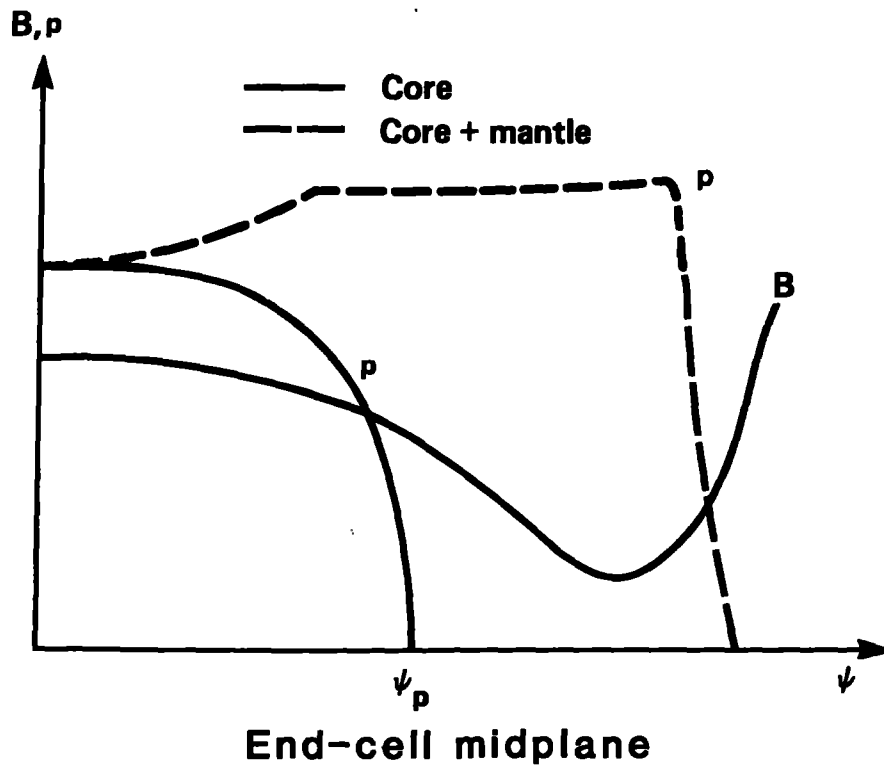
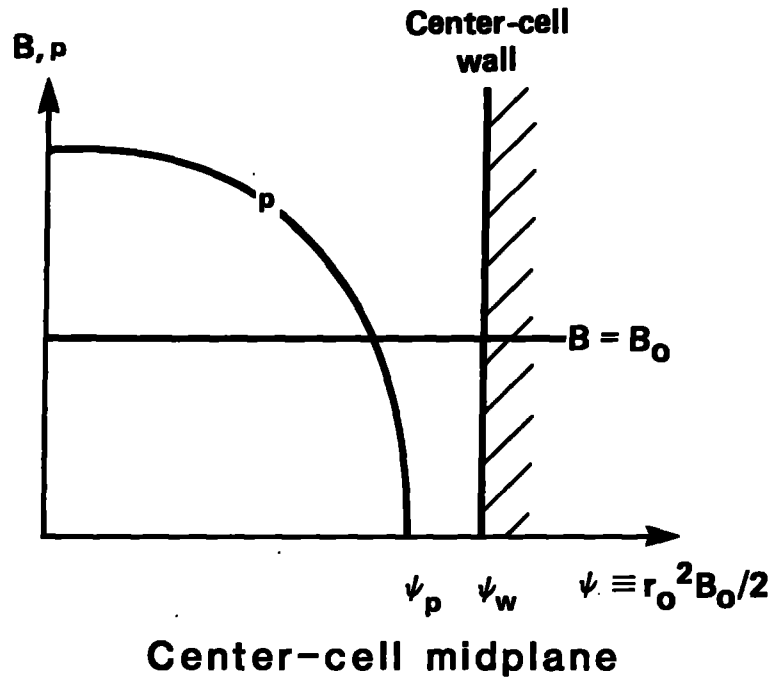


Figure 3a

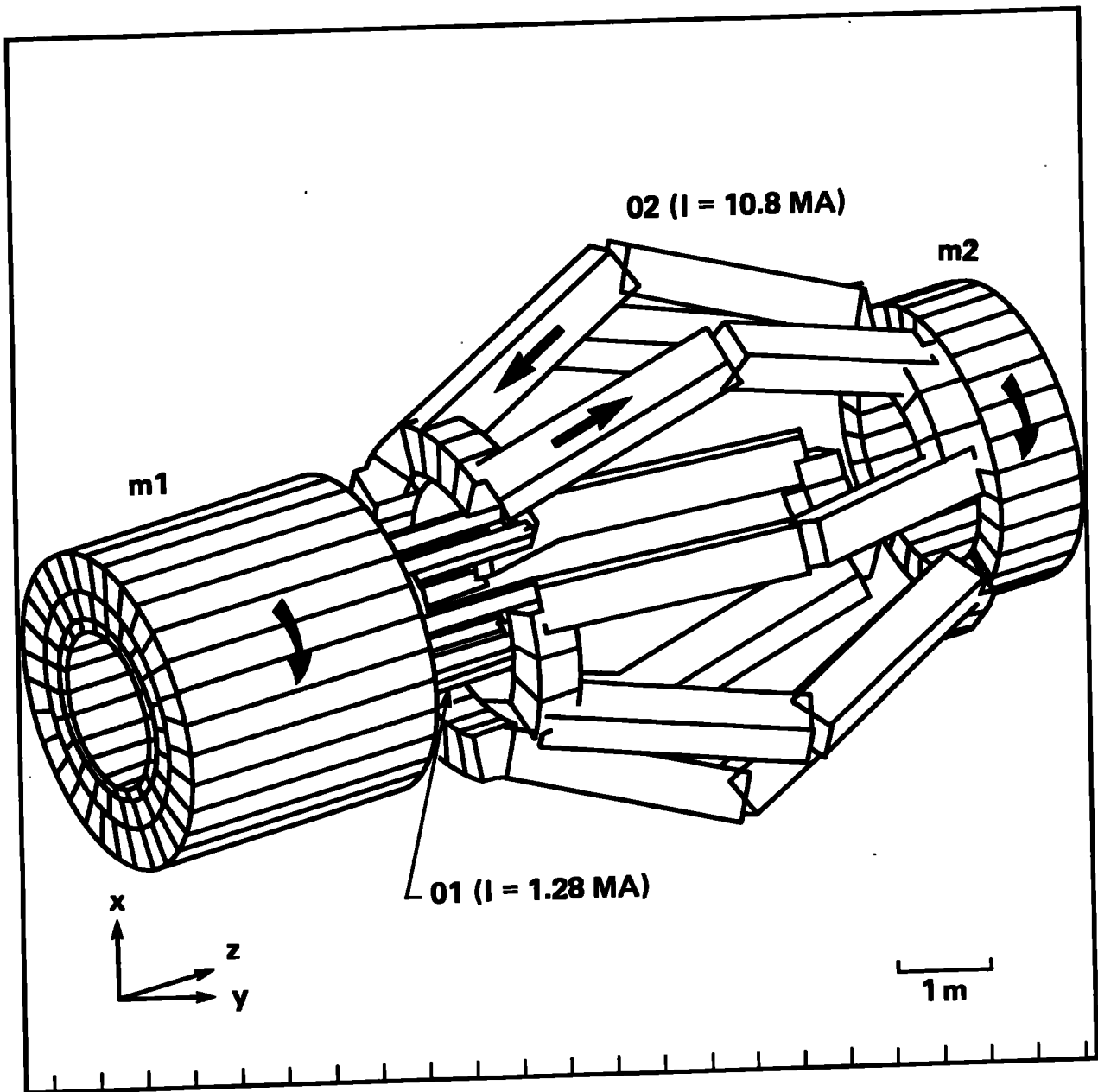


Figure 3b

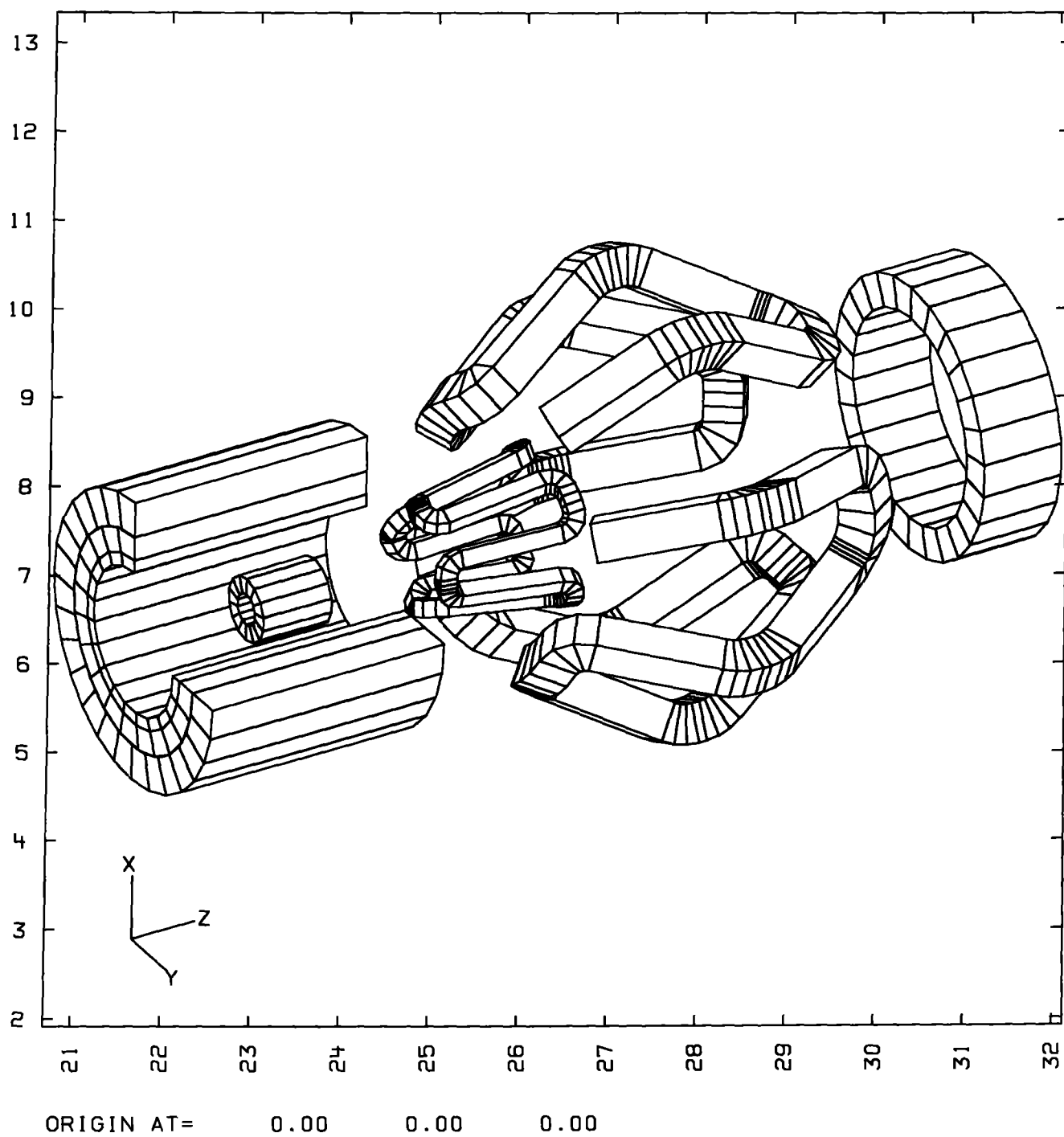
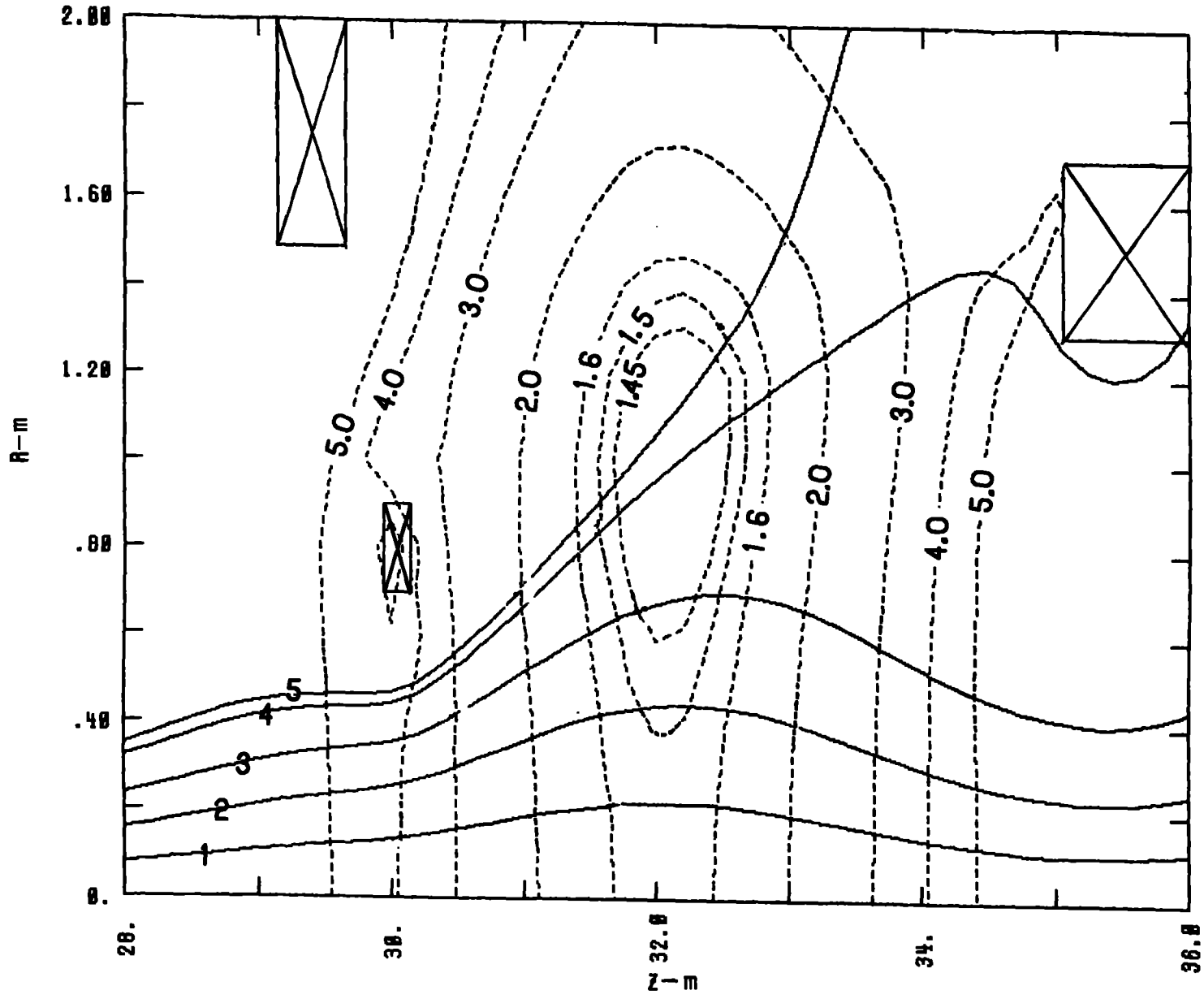


Figure 4



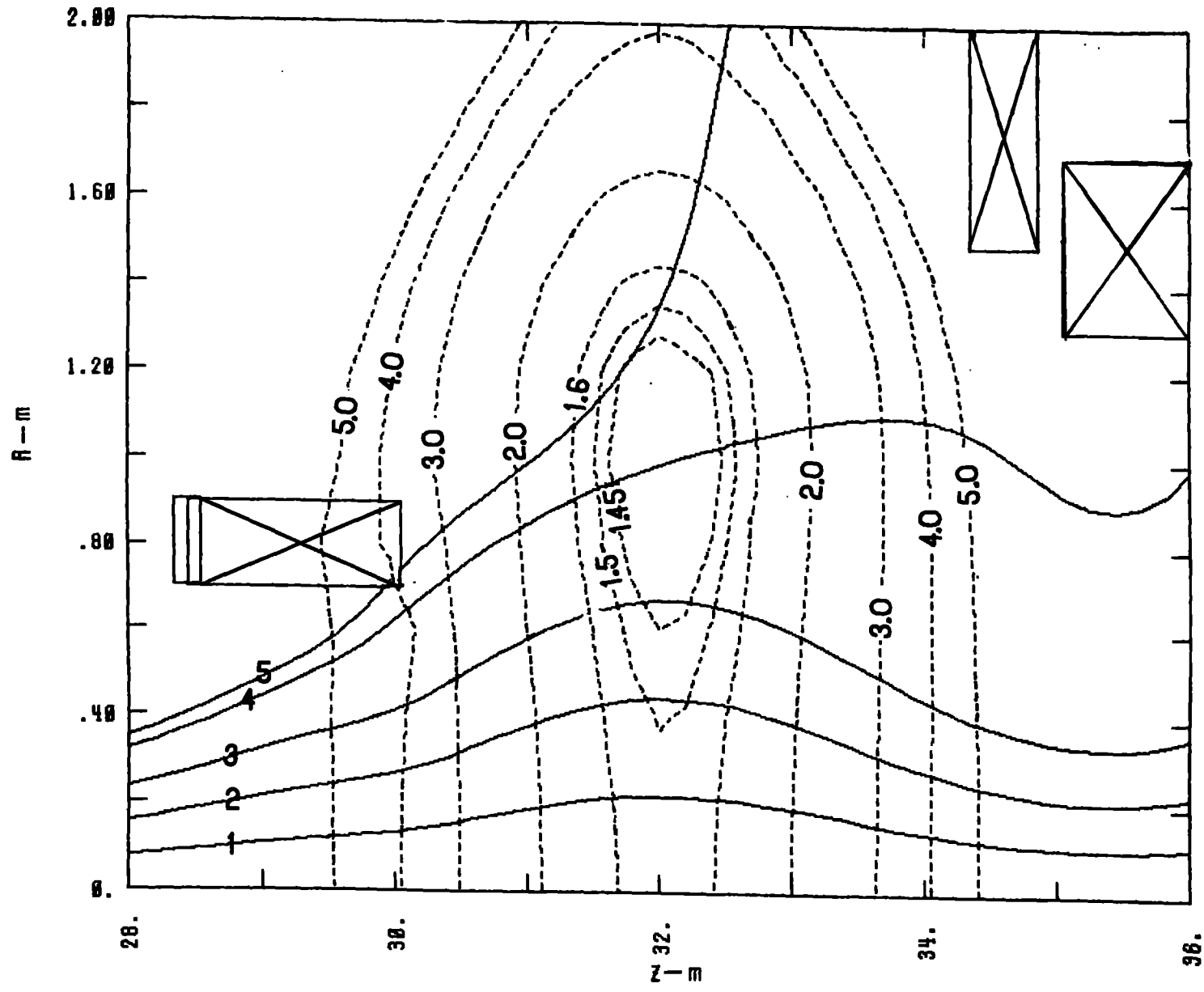


Figure 5

Figure 6

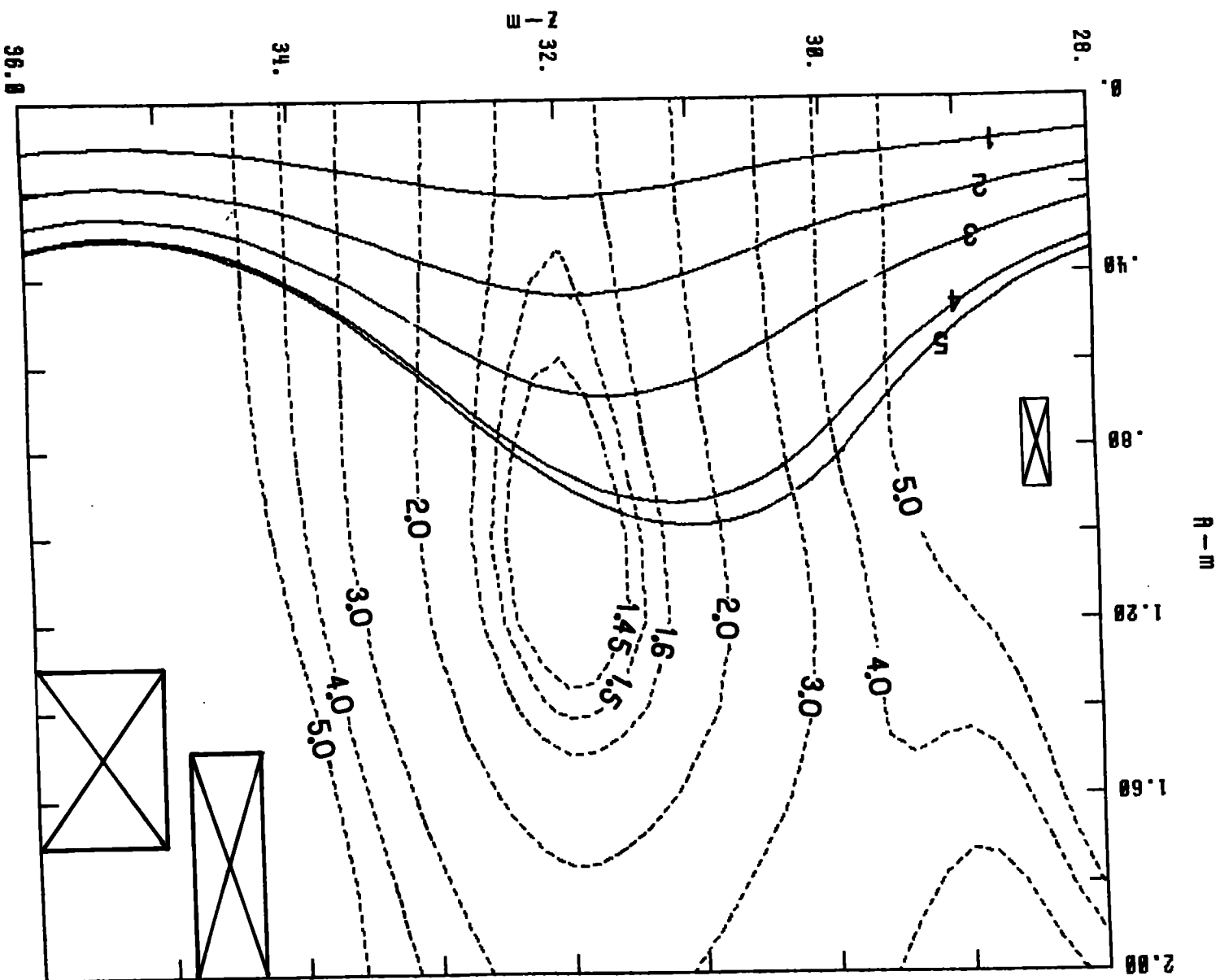
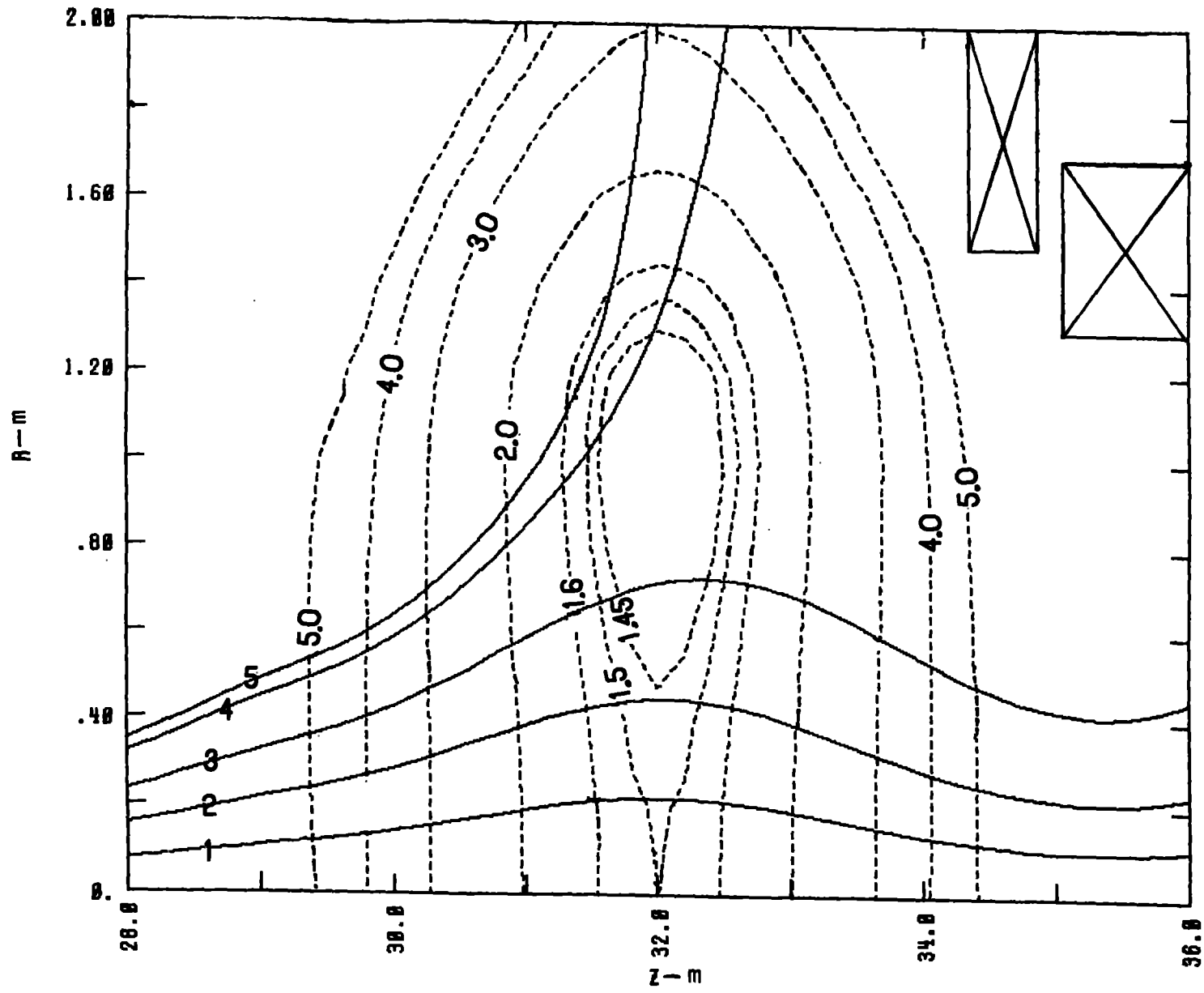


Figure 7





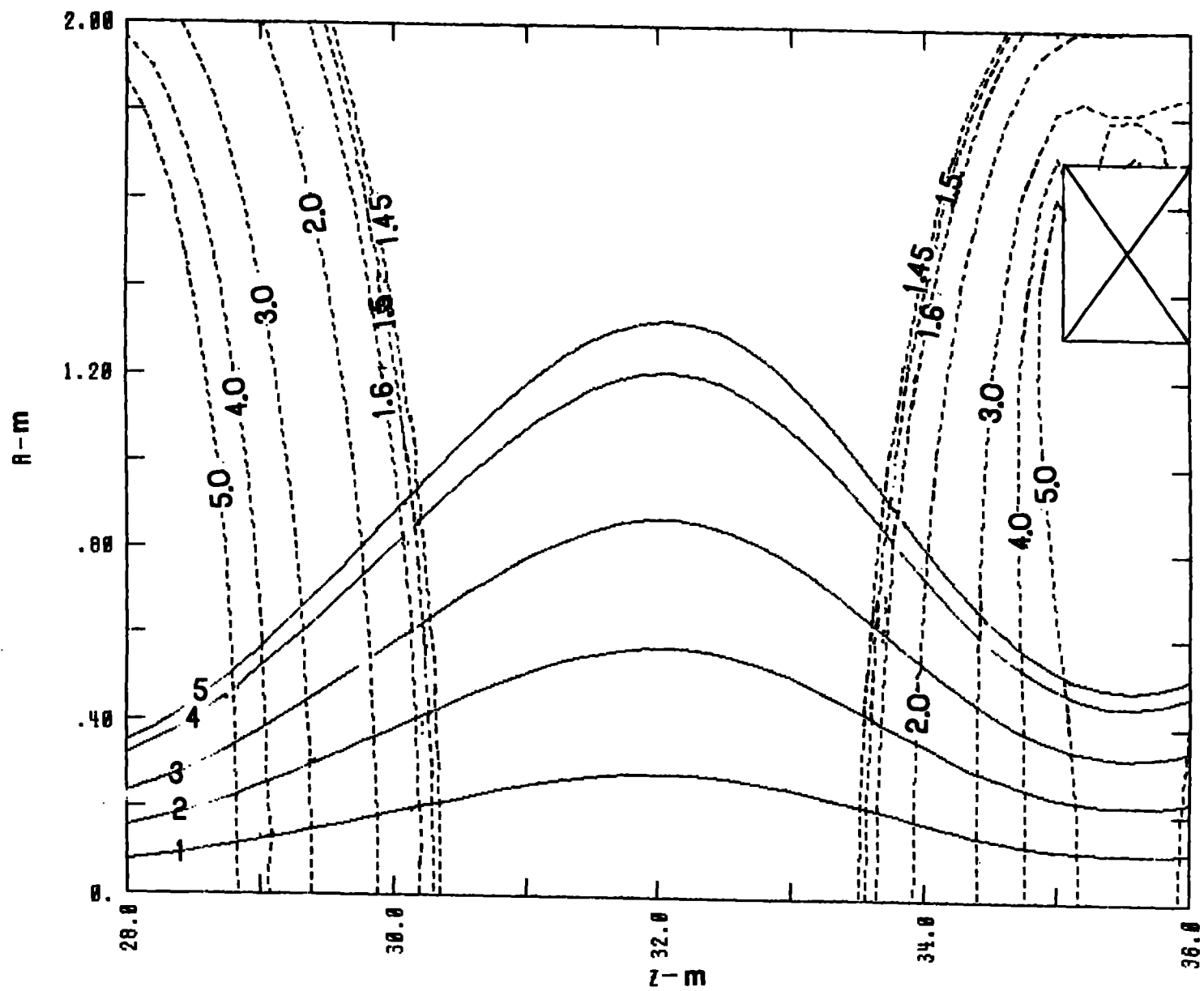
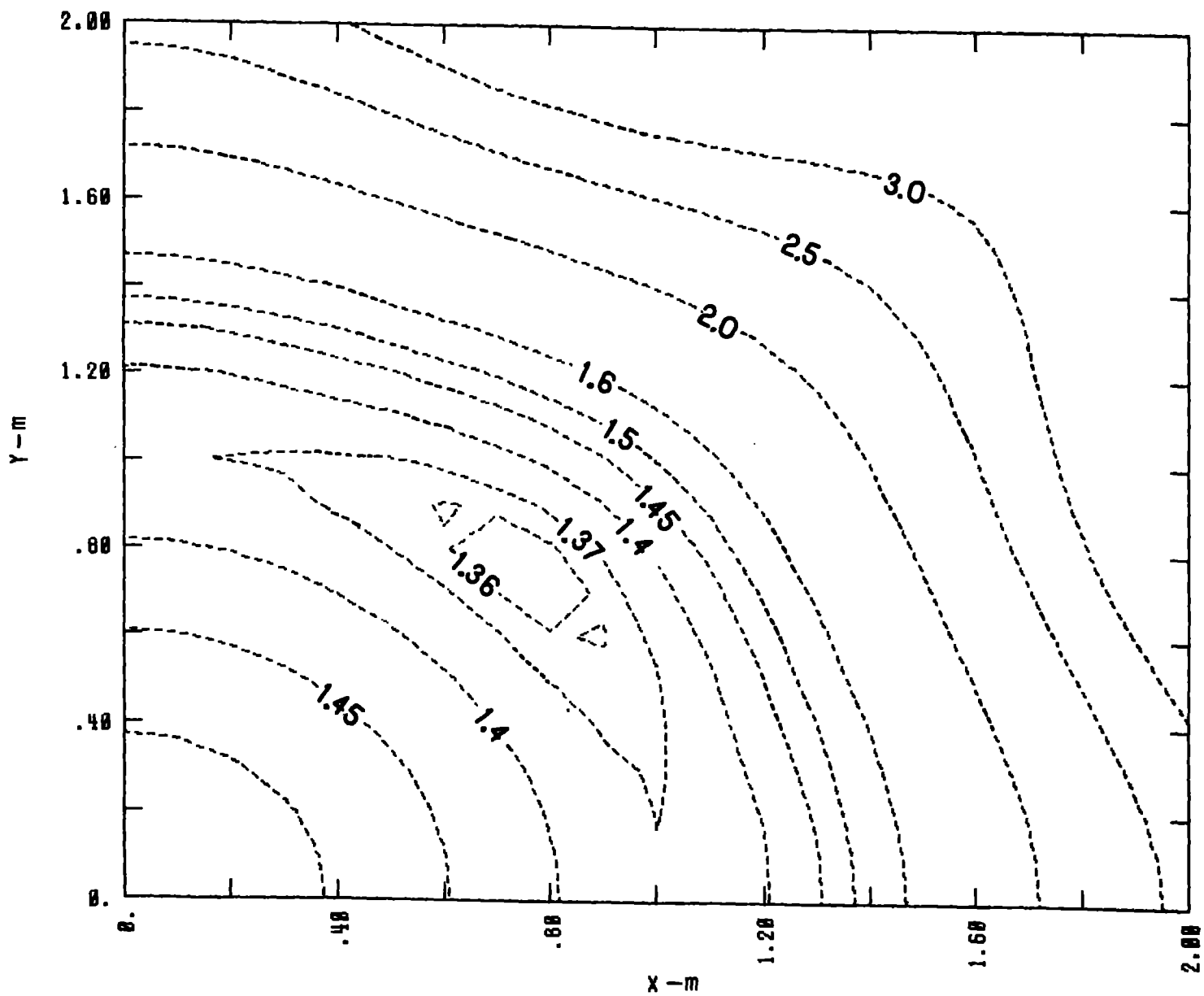


Figure 8

Figure 9



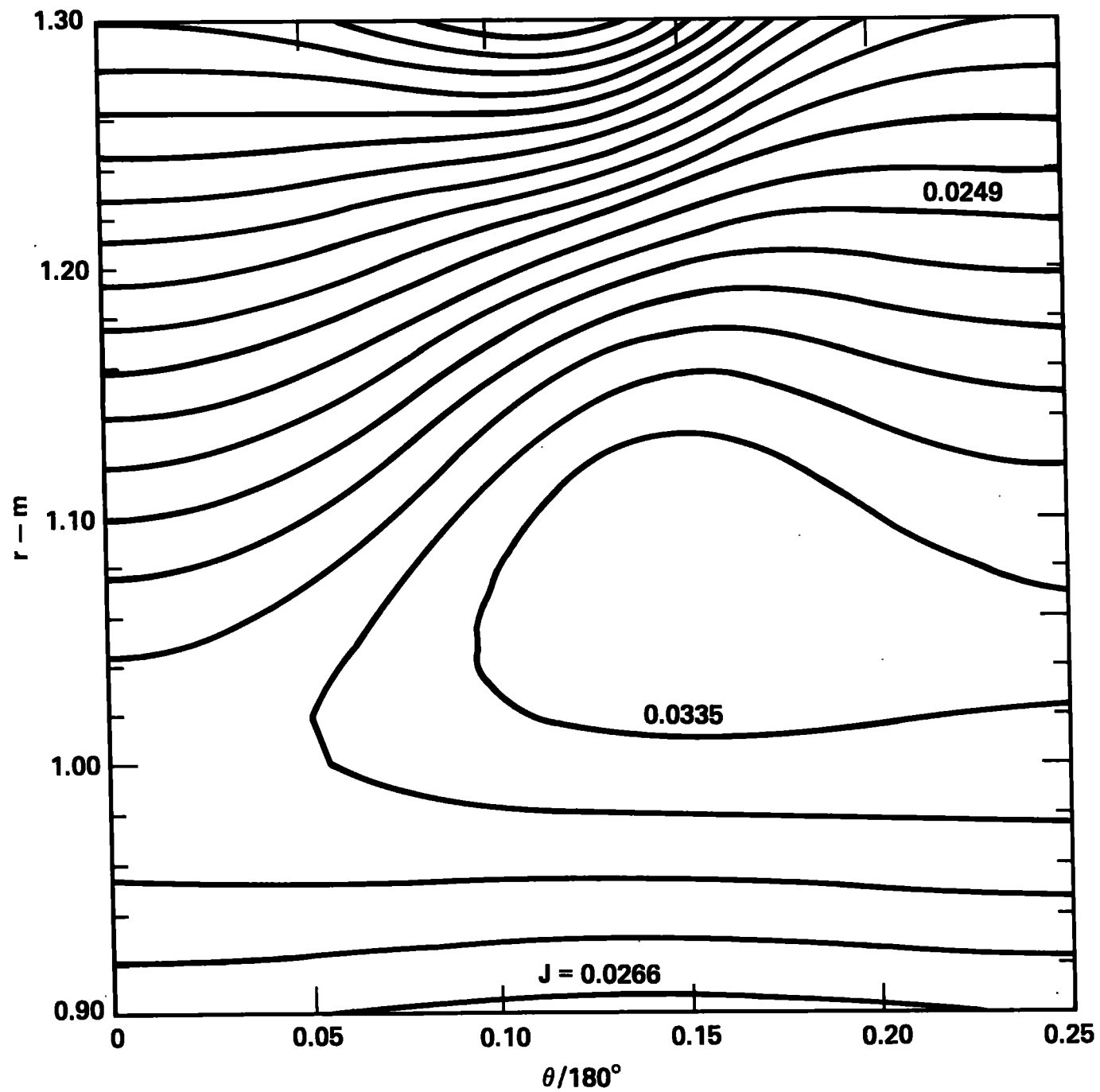


Figure 10

Figure 11

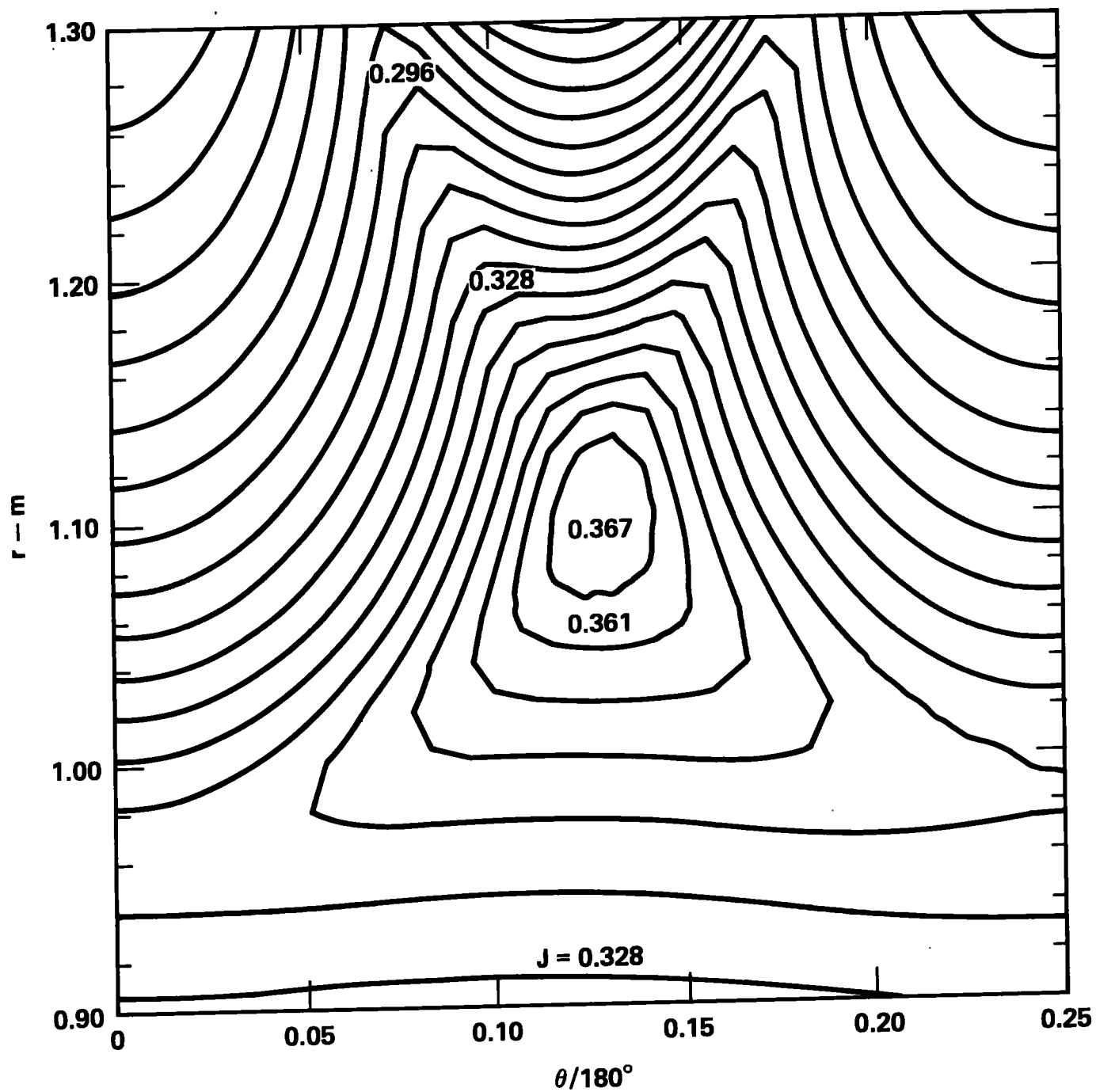


Figure 12

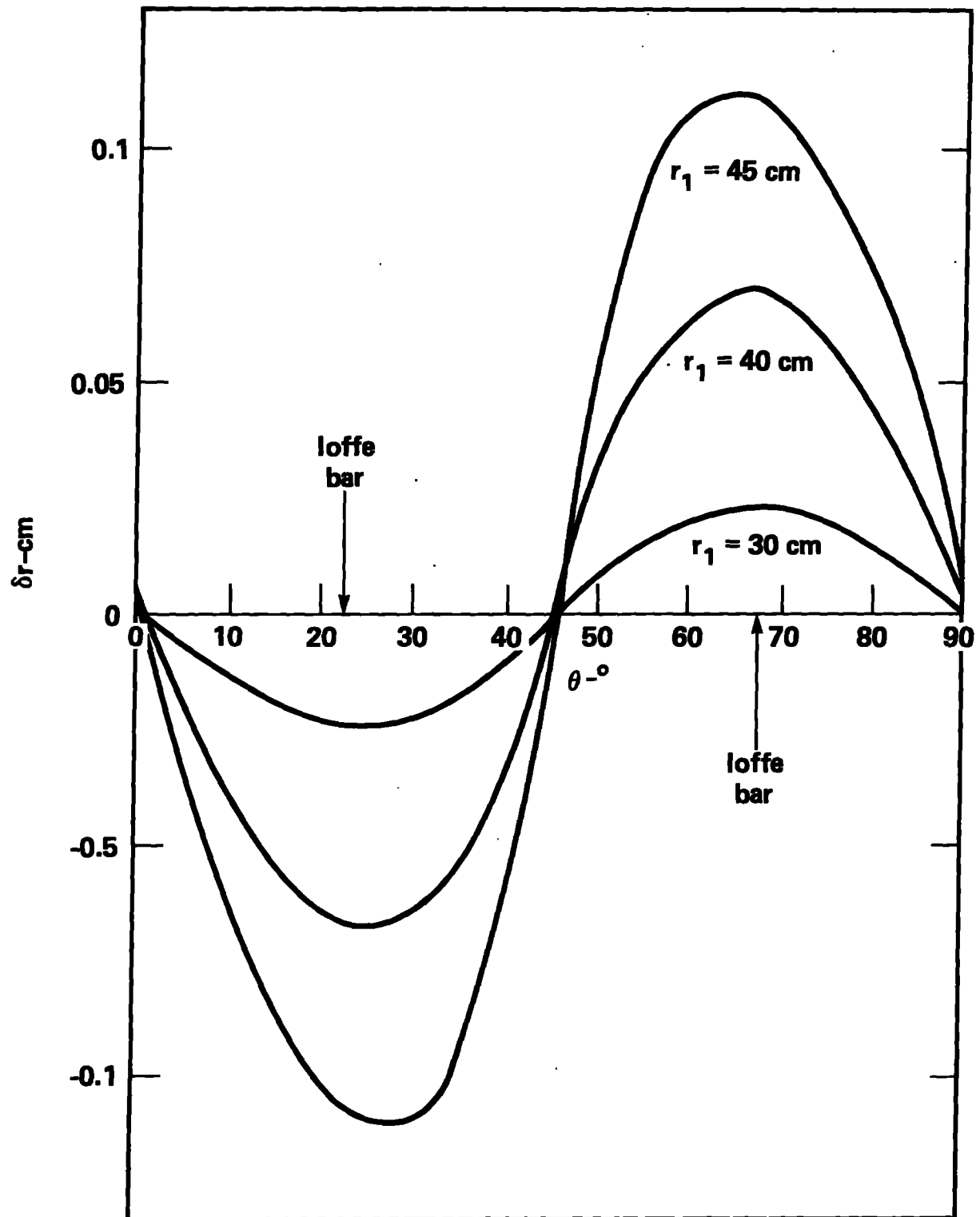


Figure 13

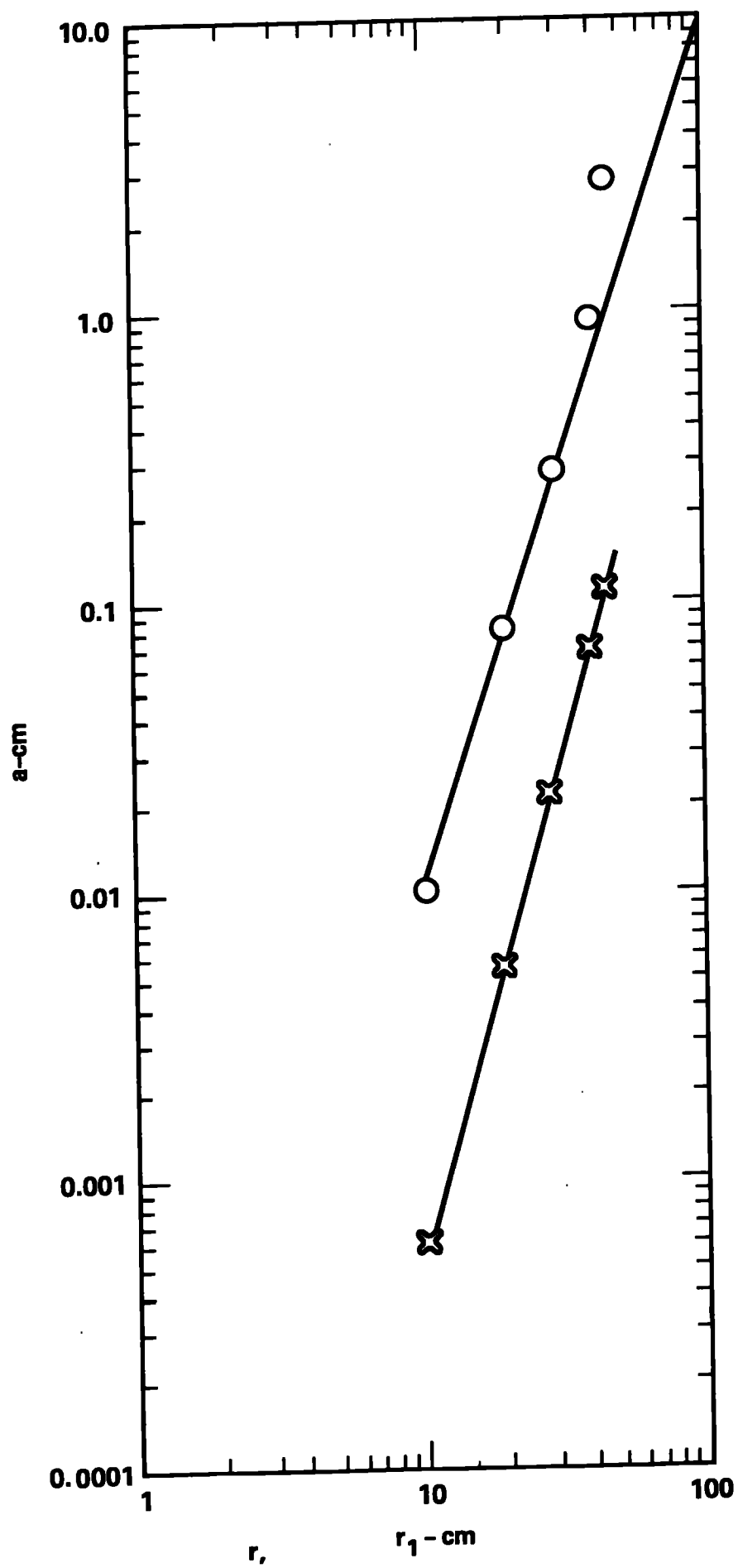


Figure 14

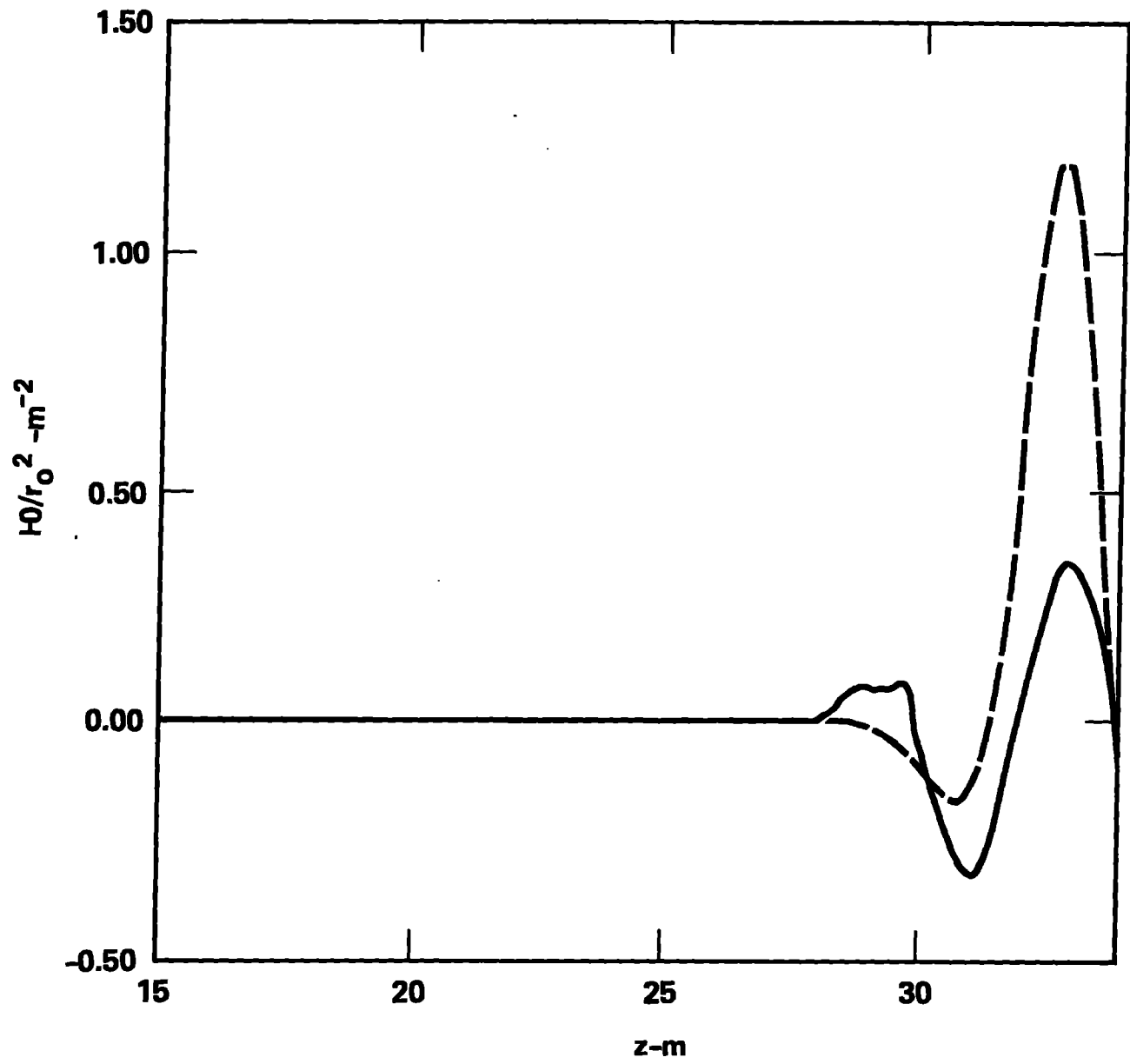


Figure 15

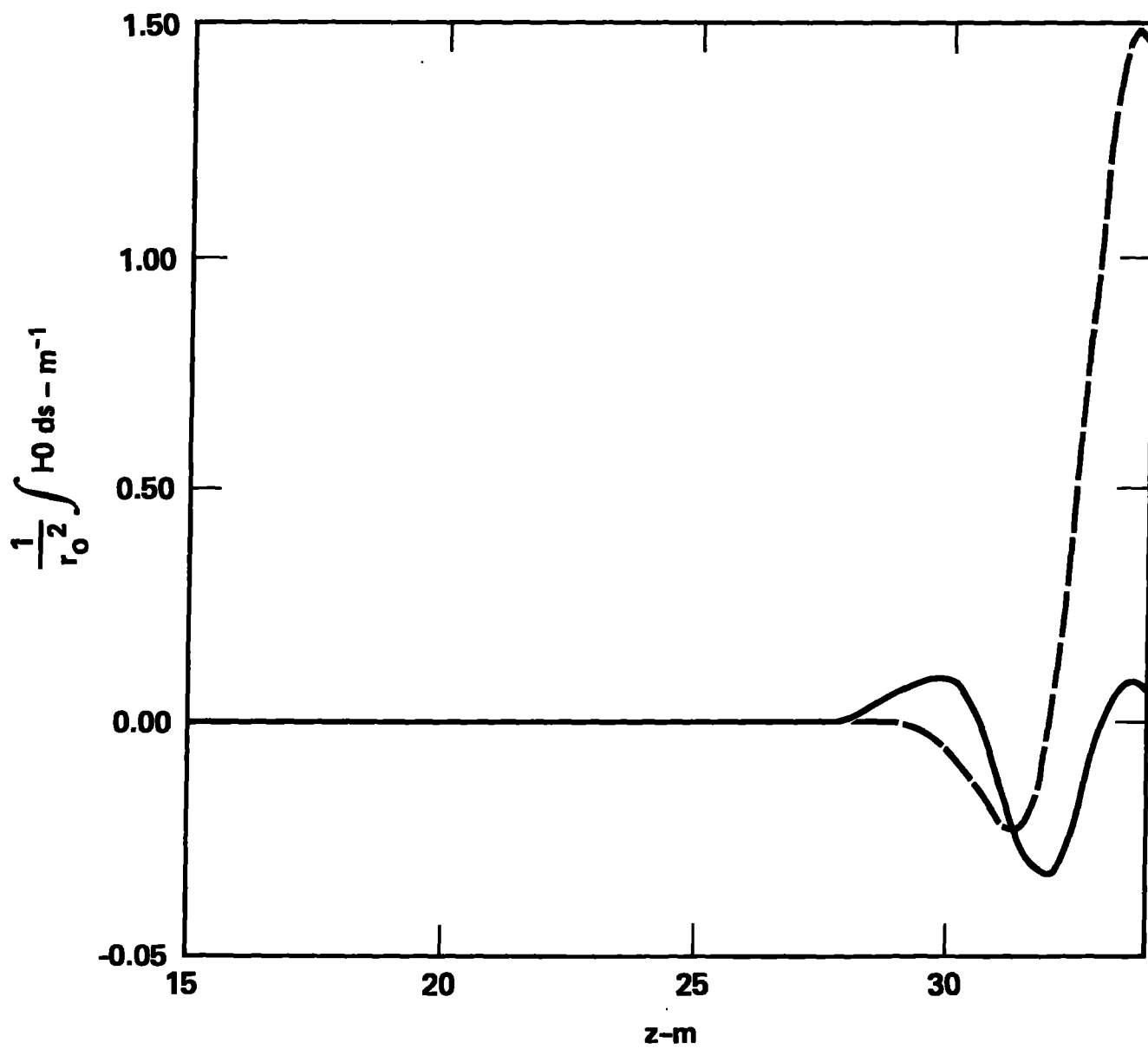




Figure 16

-55-

